EUROPEAN ORGANIZATION FOR NUCLEAR RESEARCH

SCATTERING OF NEGATIVE PIONS ON HELIUM

F. Binon[1], P. Duteil[2], M. Gouanère[3], L. Hugon[4]*,
J. Jansen[2]†, J.-P. Lagnaux[1], H. Palevsky[2]††, J.-P. Peigneux[3],
M. Spighel[3] and J.-P. Stroot[1]

IISN(Belgium)-IPN(Orsay) Collaboration

ABSTRACT

Differential cross-sections for negative pion scattering on ^{4}He have been measured at five pion kinetic energies between 110 MeV and 260 MeV in the angular range from 5° to 180°. Total cross-sections have also been measured at eleven energies between 67 MeV and 285 MeV. The differential cross-sections have been fitted with a phenomenological expression for the nuclear scattering amplitude. Conventional phase shifts have been reconstructed starting from the parameters of the fits.

Geneva - 1 June 1977

(Submitted to Nuclear Phys. B)

---

1) Institut Interuniversitaire des Sciences Nucléaires, Belgium.

2) CERN, Geneva, Switzerland.

3) Institut de Physique Nucléaire, Faculté des Sciences, Orsay, France. Present address: LAPP, Annecy, France.

4) Faculté des Sciences, Clermont-Ferrand, France.

* Now at Institut Universitaire de Technologie, Montluçon, France.

† Now at SIN, Villigen, Switzerland.

†† Permanent address: BNL, Upton, NY, USA.

1. INTRODUCTION

This work continues the pion-nucleus scattering studies at the CERN Synchro-cyclotron, which started with extensive $\pi^- - {}^{12}C$ measurements [1,2].

Negative pion elastic scattering on ^4He has been measured at five pion kinetic energies between 110 MeV and 260 MeV in the angular range from 10° to nearly 145° in steps of 5° (lab. system). Very forward angular distributions (down to $\sim 4°$) have also been measured at 110, 180, and 260 MeV and cover the angular region in which Coulomb and nuclear scattering amplitudes interfere in a measurable way. The 180° pion scattering cross-sections have been deduced from measurements made on the forward recoiling α particles.

Besides the angular distributions, total cross-sections have also been measured at eleven energies between 67 MeV and 285 MeV.

The experimental methods are reported in the first part of this article. Since the original pion spectrometer has already been described previously [1,2], only the modifications made to that set-up are discussed here. In particular, the important modifications needed to enable the momentum analysis of the recoiling α particles by the spectrometer, including the installation of low-pressure MWPC, are considered in some detail. A brief description of the helium target is also given.

The elastic differential cross-sections are reported in Section 3 together with the methods which were used for data-taking and processing.

The same is done for the total cross-sections in Section 4.

In Section 5, a phenomenological parametrization of the nuclear scattering amplitude is introduced. It explicitly takes into account the position and depth of the zeros of the amplitude as revealed by the dips in the experimental angular distributions. Using this nuclear amplitude, fits of the measured differential cross-sections, including available low-energy data around 60 MeV, are satisfactory over the complete angular range at all energies. The calculated parameters are given in tabular form. In particular, the values of ρ, the ratio of the real to the imaginary part of the forward nuclear amplitude, are compared with those predicted by forward dispersion relations. With the use of the parameters of the fits, the phase shifts are easily reconstructed. The usual ambiguities of phase-shift analysis are readily resolved at low energy. Going up in energy, a continuity argument allows the selection of a set of phase shifts which shows a reasonably smooth behaviour in the complex plane.

2. EXPERIMENTAL EQUIPMENT AND METHODS

The double achromatic spectrometer used for the measurements has been described previously [1,2]. Thus, only the main changes which were made to the original set-up are mentioned here.

2.1 Helium target

When filled with liquid helium, the target is used in the supercooled mode, which means that the pressure above the liquid is maintained at a value greater than the saturated vapour pressure. This makes sure, as was directly observed, that no inhomogeneities (bubbles) develop inside the liquid, which could lead to an erroneous evaluation of the density. In order to maintain the system in a steady supercooled régime, both the pressure and the temperature of the target have to be kept constant.

As usual, the gross cooling is ensured by liquefying helium inside the target through good thermal contact with a "cold finger" coming out of a large dewar containing liquid helium at room pressure ($\sim$ 4.2°K). A precise feedback temperature regulation system allows the maintenance of the temperature at some well-chosen value, namely (4.46 ± 0.02)°K, by enabling a forced circulation of liquid helium at 4.2°K in a spiral coil surrounding the "neck" of the target container. The helium circulation is controlled by the saturated vapour pressure (900 Torr) of a small quantity of liquid helium contained in a cavity inside the copper frame of the target itself (gas thermometer). The pressure on the liquid helium in the target is maintained at (1010 ± 10) Torr. The resulting density of the helium liquid in the target is (0.121 ± 0.001)g/cm^3.

The target can be rotated around the vertical axis in order to bring its own axis along the bisectrix of the scattering angle while, through a vertical displacement, the target itself or an empty dummy may be brought into the beam. Both movements are remotely controlled whilst the target is under high vacuum conditions.

For the angular distribution measurements, the target container itself consists of a copper frame, with 210 × 40 × 30 mm^3 inside dimensions, closed by two windows of 0.13 mm thick mylar each for the very forward measurements and 0.03 mm thick havar each for the "large-angle" measurements. Havar is a cobalt-base high-strength alloy*) with a mean Z of 26, which can be manufactured in very thin foils. These two materials have very different Coulomb differential cross-sections. The use of mylar during the forward angle measurements allows a large over-all background reduction (low Z effect). The use of havar at large angles

*) Patented Hamilton Precision Metals, Lancaster, USA.

brings most of the spurious scattering due to the windows into the low angular region (form factor effect).

The same target frame is used for the measurements of forward-emitted α particles, but the windows are 0.025 mm thick titanium foils. Of course, the target is filled, in this case, with gaseous helium in order to allow the α particles to leave the target. At each pion incident momentum, temperature and pressure are chosen such that the momentum straggling of the outgoing α particles, owing to scattering at different depths in the target, is of the same order of magnitude as the momentum acceptance of the spectrometer.

The target used for total cross-section measurements consists of a hollow copper cylindrical frame, 60 mm long and 80 mm inside diameter, closed by two 0.03 mm thick havar windows. It is filled with liquid helium at the same temperature and pressure as for the pion-scattering measurements.

The internal pressure in the target makes the windows bulge so that the effective liquid helium thickness appreciably differs from its nominal value. A precise measurement of the deformation of the windows at low temperature under given pressure conditions being rather difficult, the effective thickness is determined from measurements made at room temperature under controlled pressure conditions on the assembled target. They are extrapolated to low temperature by merely taking into account the linear dilatation of the various materials. This process leads to a relative error of ±3% on the thickness of the target used for the angular distribution measurements and to a 1% error on the thickness used for the total cross-section measurements. This error is the main contribution to the systematic error on the given cross-sections.

2.2 Angular distribution measurements

2.2.1 Forward angle measurements

The counters, the electronics, and the data-acquisition system are essentially the same as those used for the measurements on ^{12}C [2]. A sketch of the double achromatic spectrometer with the positions of the different counters is given in Fig. 1. As compared to the old set-up [2], only the anticoincidence counter $\bar{A}_2'$ is modified: the hole is now 30 × 30 mm^2 and the counter is placed at a distance of 165 mm from the centre of the target.

The trigger is given by the combination $A_1\bar{A}_1'A_2\bar{A}_2'BCD$ and the monitor by $A_1\bar{A}_1'A_2\bar{A}_2'$. The momentum dispersion of the incident beam is $\Delta p/p = 1.8\%$. The over-all angular resolution is 1°.

Each event, after fully coding, is read into an IBM 1130 computer. It is then classified into seven histograms each corresponding to one of the seven

channels of the "wall hodoscope" H_1 (Fig. 1). Each of these seven sixty-three-channel histograms covers a 10% byte of the scattered pion-momentum spectrum.

2.2.2 Large angle measurements

For the measurements at large angles, the detection system is the same as above, except for the first electronic slit $\bar{A}_1'$ which is removed and for the DISC Čerenkov counter D which is not used.

In this case the over-all angular resolution is 2°.

2.2.3 Backward scattering

The energy of the forward recoiling α particles ranges from ∿ 20 MeV to ∿ 45 MeV, corresponding to 110 MeV and 260 MeV incident pions, respectively. Important changes are made to the second part of the spectrometer for the identification of the α particles, namely:

i) The vacuum pipe in the analyser arm is directly connected to the scattering chamber so that the path of the α particles is entirely kept under high vacuum (∿ 10^{-6} mm Hg) from the target up to the final hodoscope.

ii) The scintillator counter B is replaced by a multiwire proportional chamber (MWPC) filled with pentane at low pressure (6 mm Hg) [3].

iii) A second MWPC, of the same low-pressure type, is installed just in front of the final scintillator hodoscope, in order to perform a rough momentum analysis.

In order to tune the analyser correctly, a careful study has been made of the energy losses of the α particles in the target, in its window, and in the MWPC gas and windows. The whole process has been checked with the 8.8 MeV α line from a Th B + C + C′ source. Moreover, the identification of the α particles is strengthened by an independent measurement of their time of flight between the two MWPCs.

Owing to the low scattering cross-section and to the use of cold gaseous helium in the target (see Section 2.2), whose density is a factor 10 to 50 lower than that of liquid helium, the counting rate is extremly low, typically a few counts per hour. Even at such a low density, there is a large straggling on the energy loss inside the target and the momentum spectrum of the recoiling α particles is very broad (∿ 10%). Three settings of the analysing magnet are necessary to cover completely the elastic scattering peak.

2.3 Total cross-section measurements

Total cross-sections are measured in the usual way, i.e. by measuring the attenuation of the pion beam in a target with a set of transmission counters.

Five circular scintillation counters, each 6 mm thick and 10 mm apart from one another, are placed just behind the target, inside the scattering chamber itself. They cover a solid angle of 0.14, 0.22, 0.30, 0.38, and 0.46 sr, respectively. They are put in order of increasing dimensions. This greatly simplifies handling the multiple scattering corrections.

A DISC Čerenkov counter, tuned to detect pions only, is placed in the incident beam at 102 cm from the centre of the absorption target.

Two small counters, each 1 cm in diameter, placed at 16.5 cm and 76.5 cm from the centre of the target, respectively, are defining the incident beam.

3. ELASTIC SCATTERING

3.1 Measurements where the pion is detected

3.1.1 Corrections made to the raw data

The seven histograms mentioned previously (Section 2.2.1) are treated separately. Corrections are applied for the following effects:

i) Background under the elastic peak due to the scattering of pions on the target walls. This background is measured with an empty target at a series of angles. The counting rate has been found to vary smoothly with the scattering angle. The background above 30° is negligible, except in the region of the minima in the cross-sections.

ii) Background under the elastic peak due to pion-decay muons. This background is deduced from measurements made at small angles with and without the DISC counter at the end of the beam. It is in good agreement with the result of a Monte Carlo calculation, which takes into account the exact structure of the final hodoscope. This background must only be taken into account at large angles, when no DISC is used in the trigger.

iii) Absorption of the scattered pions in the target and in the various counters. This effect amounts to 3 to 4%.

iv) Finite angular acceptance of the spectrometer. This correction can be written as

$$C_{FA} = \left\{ \frac{1}{\mathrm{tg}\ \theta} \frac{d}{d\theta} \left(\frac{d\sigma}{d\Omega}\right)_M + \frac{d^2}{d\theta^2} \left(\frac{d\sigma}{d\Omega}\right)_M \right\} \frac{\langle \theta_s^2 \rangle}{2} ,$$

where $(d\sigma/d\Omega)_M$ is the measured cross-section at the scattering angle θ, and $\sqrt{\langle \theta_s^2 \rangle}$ is the angular resolution of the analyser. This correction is subtracted from the measured cross-section in order to get the true cross-section. A measurement of the angular distribution between -5° and +5°, with the target

in place, gives the combined finite angular resolution of the two parts of the spectrometer, including the contribution of the multiple scattering in the target. The angular width $\sqrt{\langle\theta_s^2\rangle}$ so obtained is 1.1° for the small-angle measurements and 1.7° for the large-angle measurements.

v) Zero angle shift for each channel. The previous measurements also allow the determination of the true 0° scattering angle for each channel of the wall hodoscope, separately.

3.1.2 Absolute normalization of the data

The relative normalization of data taken at the same energy but during different runs is obtained by comparing measurements of the cross-sections at the same fixed reference angles made with great statistical accuracy during each run.

The absolute normalization of the cross-sections is obtained by carrying out a series of calibration experiments at the same reference angles:

i) Measurement of the individual efficiency of all counters in the analyser arm. All efficiencies were nearly equal to 100%, except for counter B made of very thin scintillator (0.4 mm), for which it was found equal to about 85.5%.

ii) Measurement of the solid angle of the analyser with a set of diaphragms of known aperture. Its value has been found to stay constant with energy and equal to $(3.76 \pm 0.06) \times 10^{-3}$ sr.

iii) Measurement of the incident beam contamination in muons and electrons. This is known with great precision owing to a DISC counter which is placed about 1 m in front of the target.

The resulting normalization factor, which has been checked by measurements made on the transmitted beam at 0°, is considered to be accurate to ±2.7%. Taking into account the 3% error on the target thickness (see Section 2.1) the absolute normalization is believed to be known with a ±4% accuracy.

3.2 Measurements where the recoiling α particles are detected

The α particles recoiling in the forward direction have been measured at the same five energies at which pion scattering has been measured. To check the method, a measurement of α particles emitted at 16.6° has first been made at one energy. These correspond to pions scattered at 144°, the largest angle where scattered pions could be detected in the laboratory. Although all relevant experimental corrections and the Jacobian (~ 4) are properly taken into account, the results obtained by the two methods, when expressed in the c.m. system, disagree by a rather large factor. The same comparison repeated at the other energies has shown that the ratio of the cross-section measured with pions to that measured with α particles, could vary between 1.5 and 3.

A series of calibration measurements has then been undertaken to try to understand this:

i) The solid angle of the analyser has been remeasured with 8.8 MeV α particles (Th B + C + C′ source). It is found to be equal to the one measured with pions.

ii) The transmission of the analyser has been measured with a thorium source of known activity and is found equal to one. This is, as explained before, a good check on the calculations of the energy losses through the whole set of counters.

iii) The efficiency of the MWPC has been directly measured with α particles of energy between 25 and 55 MeV produced at the cyclotron of the Institut de Physique Nucléaire in Lyon. It is found to be always greater than 99%.

iv) The density of the target has been checked by measuring the number of pions scattered at 30° when the target is filled with gaseous helium and when it is filled with liquid helium. Their ratio agrees, within the experimental errors, with the ratio of the corresponding densities as they are deduced from the known temperature and pressure of the target.

Since all the above tests give expected results, it is supposed that the factor attached to the α-recoil measurements remains constant, or at least varies rather little, between 0° and 16.6° (the energy of the α particles varies less than 10% in this angular range). The following scaling has then been used:

$$\left[\frac{d\sigma}{d\Omega}\,(180°)\right]^{cm}_{\pi} = \left[\frac{d\sigma}{d\Omega}\,(146.8°)\right]^{cm}_{\pi} \times \left\{\left[\frac{d\sigma}{d\Omega}\,(0°)\right]^{cm}_{\alpha} \Big/ \left[\frac{d\sigma}{d\Omega}\,(33.2°)\right]^{cm}_{\alpha}\right\},$$

where 146.8° is the c.m. angle corresponding to the maximum angle in the laboratory at which the spectrometer could be rotated, namely 144°, and 33.2° is the corresponding angle in the c.m. system for the recoiling α particles.

3.3 Results

The results of the forward angle measurements at 110, 180, and 260 MeV are given in Table 1, and those of the large-angle measurements at 110, 150, 180, 220, and 260 MeV are given in Table 2.

The complete set of data is shown in Fig. 2 as a function of θ_{cm}, the scattering angle in the c.m. system. In Fig. 3, only the "large-angle" data (for the sake of clarity) are shown versus $t/t_{max} = (1 - \cos\theta_{cm})/2$, $|t|$ being the square of the momentum transfer in the c.m. system. If one subtracts the pure Coulomb

contribution to the cross-section for the very forward angle measurements, one gets Fig. 4 where the Coulomb-nuclear interference is clearly displayed.

The differential cross-sections show a smooth continuation of the low-energy data of Block et al. [4] and Crowe et al. [5]. Their main characteristics are:

i) The angular position of the first minimum is independent of the incident pion energy.

ii) A second minimum, which is wider than the first one, appears at 150 MeV and it moves towards smaller angles as the pion energy increases.

iii) The height of the second maximum decreases by two orders of magnitude by going through the (3.3) resonance. This is very different from the $\pi^- - {}^{12}C$ case [1] where it was found that the first minimum is approximately constant versus $|t|$ and that the height of the second maximum remains almost constant versus the pion energy.

4. TOTAL CROSS-SECTION MEASUREMENTS

4.1 Data analysis

The fraction of the beam going through each transmission counter has been measured a great number of times (typically 200), a full target measurement alternating each time with an empty target one. Let R_i be the ratio of these two sets of measurements as obtained for the i^{th} counter.

4.1.1 Treatment of the raw data

Each ratio R_i has been corrected for the following effects:

i) Pion energy loss in the target. This implies that the measured cross-section is an average over a certain energy domain of the "true" cross-section. This correction happened to be negligible in our case.

ii) Multiple scattering in the last definition counter and in the target.

iii) Pion disintegration in flight. A Monte Carlo calculation allowed correction for this effect which amounted at most to some per cent, owing to the DISC counter.

iv) Absorption in the different transmission counters.

The corrected ratios R_i are then converted into partial cross-sections using the relation $\sigma(\Omega_i) = -(1/n) \ln R_i$, where n is the target thickness in nuclei per square cm and Ω_i the solid angle subtended by the i^{th} counter.

4.1.2 Extrapolation to zero scattering angle

The five partial cross-sections $\sigma(\Omega_i)$ obtained above are related to the total cross-section σ_T by

$$\sigma(\Omega_i) = \sigma_T + \int_{\Omega_i}^{4\pi} \left[\left(\frac{d\sigma}{d\Omega}\right)_C + \left(\frac{d\sigma}{d\Omega}\right)_{C-N}\right] d\Omega - \int_0^{\Omega_i} \left[\left(\frac{d\sigma}{d\Omega}\right)_{el} + \left(\frac{d\sigma}{d\Omega}\right)_{inel}\right] d\Omega ,$$

where the indices C, C-N, el, and inel refer to single Coulomb scattering, Coulomb-nuclear interference, elastic nuclear scattering, and inelastic nuclear scattering, respectively.

The single Coulomb scattering correction offers no difficulty. The elastic scattering and Coulomb-nuclear interference contributions are deduced from the measured angular distributions (at least at some energies; for the others an interpolation is made (see Section 5) so that they can also be subtracted from σ_T. Having done this, a new value is obtained, namely

$$\sigma'(\Omega_i) = \sigma_T - \int_0^{\Omega_i} \left(\frac{d\sigma}{d\Omega}\right)_{inel} d\Omega .$$

If the values of $\sigma'(\Omega_i)$ are plotted versus t_i, the square of the four-momentum transfer for scattering to the edge of the i^{th} transmission counter ($|t_i| \approx p_{lab}^2 \Omega_i/\pi$), it is found that, within the experimental errors, $\sigma'(t_i)$ decreases linearly with t_i, the slope being small. Thus a linear extrapolation to zero scattering angle has been made. The slope of the straight line is a measure of $\left[(d\sigma/d\Omega)(0°)\right]_{inel}$.

4.2 Results

The results are given in Table 3 and are displayed in Figs. 5 and 6.

Enough positive pions were available at 110 MeV to allow a total cross-section measurement. The result is also given in Table 3 and displayed in Fig. 5.

In the same figure are also shown the total elastic cross-sections which were obtained by integrating the measured angular distributions, and the remaining total inelastic cross-sections. The total elastic cross-sections at 51, 60, 68, and 75 MeV were deduced from the data of Crowe et al. [5] (see also Section 5).

The agreement between our total cross-section results and those obtained by Wilkin et al. [6] is good at the highest energies, but it becomes very bad at 150 MeV and below ($\sim$ 10 standard deviations). Nevertheless, the difference between the π^+ and π^- total cross-sections at 110 MeV is, within the experimental errors, the same in both experiments. Below 100 MeV our data are in good over-all

agreement with the preliminary results of Burleson et al. [7]. The dashed curve is a theoretical prediction by Locher et al. [8].

5. DATA ANALYSIS AND DISCUSSION

5.1 Parametrization and fits of the differential cross-sections

Figures 3 and 4 clearly show that except for the region where nuclear and Coulomb amplitudes interfere in a significant manner, the forward nuclear scattering amplitude has an exponential behaviour versus $|t|$. A good parametrization of the nuclear amplitude is obtained in this region with an exponential function of the form $a \exp(-b|t|/2)$. On the other hand, it is also clear from these figures that it is only valid up to $t/t_{max} \lesssim 0.2$, where dips and bumps start showing up. This type of structure can be parametrized by a function of the form $\Pi_j(1 - |t|/t_j)$, where t_j are complex constants, i.e. poles in the complex plane. Their real part is linked to the position of the dips and their imaginary part to the depth of the dips.

It is thus natural to try a global parametrization of the data by just putting together these two partial parametrizations, i.e. by multiplying such a product of pole terms by an exponential function of $|t|$. In fact this was first suggested to us by Germond and Wilkin [9].

5.1.1 Parameters: definition and meaning

Warning: Henceforth, all quantities mentioned below, unless otherwise stated, refer to the c.m. system. From now on, also, the notation t for the square of the momentum transfer will be used, instead of $|t|$.

If f_C (f_N) denotes the pure Coulomb (nuclear) scattering amplitude, i.e the scattering amplitude in the absence of nuclear (Coulomb) interaction, then

$$\frac{d\sigma}{d\Omega} = \left| f_N \, e^{-2i\delta} + f_C \right|^2 ,$$

where 2δ is the relative phase, also called "Bethe phase", between the two scattering amplitudes.

i) The pure Coulomb amplitude for spin 0 - spin 0 scattering, is given by

$$f_C(t) = -2\eta \frac{k}{t} F_\pi(t) F_A(t) .$$

η, the effective Coulomb coupling constant, is given by

$$\eta = Z_1 Z_2 \alpha / \beta_{lab} ,$$

where Z_1 and Z_2 are the charges of the projectile and of the target nucleus ($Z_1 Z_2 = -2$), respectively; β_{lab} is the velocity ($c = 1$) of the projectile in the laboratory and α the fine structure constant. k and t are the momentum and the square of the momentum transfer, respectively.

The functions $F_\pi(t)$ and $F_A(t)$ are the pion and the nucleus form factors, respectively. For $F_\pi(t)$ the standard form

$$F_\pi(t) = \exp\left[-r_\pi^2 t/6\right]$$

is used where $r_\pi = 0.8$ fm is the value taken for the r.m.s. radius of the pion. For helium the following expression [10] is adopted

$$F_{He}(t) = \left[1.0 - 0.9986 \times t\right]^6 \exp\left[-0.4638 \times t\right] ,$$

which for small t values is well approximated by

$$F_{He}(t) \simeq \exp\left[-r_{He}^2 t/6\right] ,$$

where $r_{He} = 1.67$ fm is the r.m.s. radius of helium.

ii) The parametrization of the nuclear scattering amplitude, as introduced above, is explicitly written

$$f_N(t) = f_N(0) \exp\left[-R_s'^2 t/6\right] \prod_{j=1}^{J} (1 - t/t_j) .$$

The forward amplitude $f_N(0)$ is written, as usual, as

$$f_N(0) = \frac{k}{4\pi} \sigma_{tot}\left[i + \rho\right] ,$$

where $\rho = \mathrm{Re}\, f_N(0)/\mathrm{Im}\, f_N(0)$. The t_j are complex constants (poles) and J is the number of dips in the angular distribution.

For small t values, f_N reduces to

$$f_N(t) \simeq f_N(0) \exp\left\{-\left[R_s'^2/6 + \sum_{j=1}^{J} (1/t_j)\right] t\right\} ,$$

which allows for the definition of an effective strong interaction r.m.s. radius

$$R_s^2 = R_s'^2 + 6\, \mathrm{Re}\left[\sum_{j=1}^{J} (1/t_j)\right] .$$

It is convenient to introduce the notation $t_j = 2k^2(1 - z_j)$, where z_j are new complex constants. R^2 can then be written

$$R_s^2 = R_s'^2 + \frac{3}{k^2}\left[\sum_{j=1}^{J} \mathrm{Re}\ (1 - z_j)^{-1}\right] .$$

iii) The relative phase 2δ is given by [11]

$$2\delta = -\eta\left\{\ln\left[(R_s^2 + r_\pi^2 + r_{He}^2)t/6\right] + 0.5772\right\} .$$

5.1.2 Fits of the differential cross-sections: results

Our measured differential cross-sections, together with those of Crowe et al. [5] at lower energies, have been analysed according to the above-mentioned formalism with only ρ, R_s', and the z_j as free parameters. Fitting was done by using the powerful minimization program MINUIT [12], a Library Program on the CERN CDC 7600.

The results of the fits are given in Table 4. The values of σ_{tot} used in the fits are those measured in this experiment except for the one at 75 MeV, which was obtained by interpolating our results, and those at 51 and 60 MeV which result from an extrapolation of our data, assuming that the total cross-section goes smoothly to zero with T. Since this is a quite arbitrary, although plausible hypothesis, rather large errors have been taken in both of these cases.

The error quoted for each parameter results from the statistical combination of three different errors: the standard error given by the program MINUIT (which corresponds to a change of the χ^2 from χ^2_{min} to $\chi^2_{min} + 1$), the error coming from the ±4% uncertainty in the absolute scale of the differential cross-sections, and the error resulting from the propagation in the fits of the error on the total cross-sections.

The slight difference (essentially on ρ) between the values of the parameters given here, in Table 4, and those given in a previous paper [13] comes from a small change in the relative phase 2δ, where R_s' was taken instead of R_s.

The final parameters can be interpreted as follows:

i) The knowledge of ρ gives immediately the values of Re $f_N(0)$ which are shown in Fig. 7. The curves shown in the same figure are results of forward-dispersion-relation calculations made by Wilkin et al. [6] (dashed curve) and by Batty et al. [14] (full curve). There is a fair agreement between theory and experiment for all but the highest energies, where a rather large discrepancy shows up.

ii) Starting from the values given in Table 4, it is easy to calculate the square of the effective r.m.s. strong interaction radius at zero momentum transfer

$$R_s^2 = R_s'^2 + \frac{3}{k^2} \sum_{j=0}^{J} \frac{\mathrm{Re}\ (1 - z_j)}{|1 - z_j|^2} .$$

It has been shown by Beiner and Germond [15] and Silbar and Sternheim [16] that π-nucleus elastic scattering can be well described by a simple optical-model potential if an energy-dependent effective radius is used. For an amplitude which behaves like $P_\ell(\cos\theta)$, the effective radius is given by [16]

$$R^2 = R_A^2 + \frac{3}{2}\,\ell(\ell + 1)\,\frac{1}{k^2} ,$$

where R_A is the r.m.s. radius of the nuclear density, or r.m.s. "matter radius", which in the case of ^{4}He is equal to

$$R_{He}^2 = (1.67)^2 - (0.8)^2 = (1.47)^2 .$$

In particular for a pure p-wave, the above formula becomes

$$R^2 = (1.47)^2 + \frac{3}{k^2} .$$

In the case of π-nucleus scattering around the 3/2, 3/2 resonance, where the p-wave is known to play a dominant role, R_s^2 is expected to follow rather closely the above relation. This is actually the case, as may be judged from Fig. 8 where the calculated values of R_s^2 are plotted versus $1/k^2$. A linear least-squares fit to the data gives

$$R_s^2 = (1.631 \pm 0.075)^2 + (3.78 \pm 0.15)/k^2 ,$$

when all points are taken into account (full curve) and

$$R_s^2 = (1.552 \pm 0.027)^2 + (4.40 \pm 0.12)/k^2$$

when only the data between 110 MeV and 260 MeV are fitted (dashed curve). The agreement with the effective radius formula given above is surprisingly good as a linear fit supposes that one partial wave enters into account only. It will be seen later (Section 5.2) that this is not the case. Moreover, the coefficient of $1/k^2$ varies rapidly with ℓ: it is 0, 3, 9, 18, ... for ℓ = 0, 1, 2, 3, ..., respectively.

iii) In Fig. 9 are shown the values of $\mathrm{Re}\ t_j = 2k^2\ \mathrm{Re}\ (1 - z_j)$ together with their physical limit ($4k^2$). They show a very regular behaviour, the "trajectory" of $\mathrm{Re}\ t_2$ being nearly parallel to the one of $\mathrm{Re}\ t_1$. The large error bar for $\mathrm{Re}\ t_2$ at 150 MeV reflects the difficulty encountered by the fitting program to

find the location of the second dip. However, it is quite remarkable that it is impossible to get a good χ^2 at 150 MeV without introducing a second dip in the fitting process.

iv) A major difficulty is encountered for the determination of the sign of Im t_j = $2k^2$ Im $(1 - z_j)$. Equally good fits are obtained with both signs. The origin of this ambiguity in sign can be found by developing the expression for the differential cross-section in the following manner:

$$\frac{d\sigma}{d\Omega} = |f_N\, e^{-2i\delta} + f_C|^2 =$$

$$= |f_N|^2 \left\{ 1 + \frac{|f_C|^2}{|f_N|^2} + 2\,\frac{|f_C|}{|f_N|}\,\frac{\text{Re } f_N}{|f_N|}\left[\cos(2\delta) + \frac{\text{Im } f_N}{\text{Re } f_N} \sin(2\delta) \right] \right\}.$$

Reading in Fig. 8 the values of R_s^2, it is easy to calculate the value of 2δ in the region of the first dip ($\theta_{cm} \approx 75°$). It is found that 2δ varies between 0.035 at 260 MeV and 0.022 at 51 MeV, which means that cos $(2\delta) \approx 1$ and sin $(2\delta) \approx 0.03$ in that energy domain, at the position of the first dip. Using the values of Table 4, it can also be verified that Im f_N/Re f_N is of the order of unity in that region. Thus even when $|f_C|$ and $|f_N|$ are of the same order of magnitude, the cross-section is insensitive to the sign of Im f_N, because the latter appears only in the product term Im f_N sin (2δ)/Re f_N which is small compared to cos (2δ). This stresses again the importance of having a good theoretical estimate for the phase 2δ at large momentum transfers. In that respect, it is perhaps good to recall that the expression given above for 2δ is well justified theoretically for small t values, but still lacks justification at high momentum transfers.

Since the sign of Im $(1 - z_j)$ is not fixed by the fit, the signs given in Table 4 are in a certain manner arbitrary, although not entirely so. As a matter of fact, it will be shown in Section 5.2 that from the preceding analysis it is possible to reconstruct a phase-shift analysis. The sign ambiguity for the Im $(1 - z_j)$ is closely related to the well-known ambiguities encountered in standard phase-shift analysis. However, it is univocally removed at energies up to 110 MeV, because the "reconstructed" s-wave phase shifts fall outside the unitary circle if the wrong sign is chosen. Above 110 MeV a plausible guess may be obtained by looking at the values of Im t_1 as a function of T (Fig. 10), using the argument of continuity. It is most likely that only two sets of values are physically acceptable: either all values of Im $(1 - z_1)$ are taken with the positive sign (continuous curve), or they go through zero around about 220 MeV and become negative at 260 MeV (dashed curve). As the phase shifts resulting from the first choice (continuous curve) show a somewhat more regular behaviour (see also Section 5.2) than with the other one, the signs given in Table 4 are adopted.

With regard to Im $(1 - z_2)$ one gets to the signs given in Table 4 partly by the continuity argument, partly from the smoothest behaviour observed for the phase shifts in the complex plane, though the situation is far less clear than for Im $(1 - z_1)$.

5.2 "Reconstructed" phase-shift analysis

5.2.1 Reconstruction of the phase shifts starting from the phenomenological fit

In a phase-shift analysis of the scattering of spin 0 particles, the scattering amplitude is approximated by the finite sum

$$f(\theta) = \frac{1}{k} \sum_{\ell=0}^{L} (2\ell + 1)\, a_\ell\, P_\ell(\cos\theta) \ .$$

a_ℓ are complex coefficients usually written as $a_\ell = [\eta_\ell \exp(2i\delta_\ell) - 1]/2i$, where δ_ℓ is the (real) phase-shift parameter for the ℓ^{th} partial wave and η_ℓ the corresponding (real) absorption parameter $(0 \leq \eta_\ell \leq 1)$. $P_\ell(\cos\theta)$ are the usual Legendre polynomials.

The above expression being composed of a sum of polynomials, it is itself a polynomial of degree L in cos θ. Thus a phase-shift analysis is based on a development in cos θ of the form

$$f(\theta) = \sum_{\ell=0}^{L} A_\ell \cos^\ell\theta \ .$$

This remark is at the origin of Gersten's systematic study of the ambiguities which are encountered in complex phase-shift analysis [17]

It can be shown that the phenomenological expression for f_N given previously (Section 5.1.1) can readily be written as an expansion in cos θ. To prove this, it is first noted that the exponential term can be written as exp $(-u)$ exp $(u \cos\theta)$, where $u = R_s'^2 k^2/3$, and

$$\exp(u\cos\theta) = I_0(u) + 2 \sum_{k=1}^{\infty} I_k(u) \cos(k\theta) \ ,$$

where $I_k(u)$ are (modified) Bessel functions of integer order [18]. Taking into account the fact that cos $(k\theta)$ can be represented as a polynomial of the k^{th} degree in cos θ, it follows that

$$\exp(-R_s'^2 t/6) = \exp(-u)\exp(u\cos\theta) = \sum_{m=0}^{\infty} b_m \cos^m\theta \ ,$$

where

$$b_0 = e^{-u}$$

$$b_1 = e^{-u} \left\{ 2 \sum_{n=1}^{\infty} (-)^{n+1} \, (2n - 1) \, I_{2n-1}(u) \right\}$$

$$b_2 = e^{-u} \left\{ 4 \sum_{n=1}^{\infty} (-)^{n+1} \, n^2 \, I_{2n}(u) \right\} ,$$

etc.

In the energy domain considered here, u varies between 0.27 at 51 MeV and 1.78 at 260 MeV, the value u = 1 corresponding nearly to T ≃ 180 MeV. Tables of exp (-u) $I_k(u)$ are given in Ref. [18].

On the other hand, since $t = 2k^2(1 - \cos \theta)$ and t_j are complex constants, the product $\Pi_{j=1}^{J}(1 - t/t_j)$ is a polynomial of degree J in cos θ. Combining the two preceding results, it follows that f_N can be written as a series of powers in cos θ, i.e.

$$f_N(\theta) = \sum_{k=0}^{\infty} C_k \cos^k \theta ,$$

where C_k are complex constants.

Comparing this last expression with the expansion in partial waves, it is clear that if both expressions are to represent the same physical situation for every cos θ, then they must be limited to the same power L of cos θ and

$$A_j = C_j \quad \text{for} \quad 0 \leq j \leq L ,$$

which allows one to express the phase-shift parameters as functions of the parameters of the phenomenological fit. For example, for a phase-shift analysis limited to 5 partial waves (L = 4) the identification gives

$$\begin{cases} a_4 = k \, \frac{8}{315} \, C_4 \\ a_3 = k \, \frac{2}{35} \, C_3 \\ a_2 = k \, \frac{2}{15} \left(C_2 + \frac{6}{7} \, C_4 \right) \\ a_1 = k \left(\frac{1}{3} \, C_1 + \frac{1}{5} \, C_3 \right) \\ a_0 = k \left(C_0 + \frac{1}{3} \, C_2 + \frac{1}{5} \, C_4 \right) . \end{cases}$$

5.2.2 Results

A program has been written which does those calculations taking into account eight partial waves (L = 7). As δ and η are becoming very small for $\ell > 4$, only the

results for the first five partial waves are given in Table 5 and only the first four are represented in Fig. 11. In Fig. 11 are shown also the results of Nordberg et al. [19] at 24 MeV.

The phase shifts obtained at 51, 60, 68, and 75 MeV are, within the quoted errors, in good agreement with those obtained by Crowe et al. [5] through a standard phase-shift analysis.

Concerning the errors given in Table 5, a word of caution is necessary as the parameters ρ, R'_s, etc., which are implicitly contained in the coefficients C_i, have been treated as independent variables and the corresponding errors accordingly. In fact, it is clear that not all the parameters are independent, some of them being even highly correlated; for example, the correlation coefficient between ρ and R'_s can reach a value as high as ~ 0.6. However, a complete calculation of the error propagation, taking into account the correlation coefficients between all pairs of parameters, is complicated and tedious, and we did not do it. The quoted errors in Table 5 must be considered as indicative only.

Phase shifts given in Table 5 have been obtained by taking all values positive for Im $(1 - z_1)$ (full curve in Fig. 10), while all Im $(1 - z_2)$ have been taken with the negative sign. We have already mentioned (Section 5.1.2) that there is no problem in determining the sign of Im $(1 - z_1)$ at and below 110 MeV as the phase shifts obtained with opposite sign lie outside the unitary circle. This is no longer true above 110 MeV, where the sign of Im $(1 - z_1)$ is affecting enormously the value of δ_ℓ without changing much the value of the absorption parameter η_ℓ. This can be seen in Table 6, where we have given a resumé of the values taken by δ and η for the first three partial waves, and for all possible combinations of the signs of the imaginary coefficients Im $(1 - z_i)$ at energies above 110 MeV. Our choice of signs, which corresponds to the two leftmost columns in Table 6, is arbitrary, except for the fact that it is the one which gives the smoothest possible behaviour that can be found for the phase shifts in the complex plane taking into account the continuity argument for the values taken by Im $(1 - z_i)$.

5.3 Discussion

Though lacking in precision, the trajectories of the phase shifts in the complex plane (Fig. 11) show at least clearly a common tendency to cross the imaginary axis between 150 and 220 MeV, i.e. in the energy region where the π-N 3/2 3/2 resonance takes place. Now, this is the behaviour expected for π-N scattering on a nucleon bound inside a nucleus. As a matter of fact, the partial-wave expansion for pion scattering on a bound nucleon at the resonance energy, which involves only the p-wave in the pion-nucleon c.m. system, when transformed back to the nucleus c.m. system generates partial waves of various ℓ that behave

in a manner similar to the original one. So, the particular behaviour of the trajectories in Fig. 11 is a first indication that what is observed, in fact, is the formation inside the nucleus of a Δ_{33} which decays before being absorbed.

This conclusion receives further support from the fact mentioned before (Section 3.3), namely that the angular position of the first minimum is energy-independent, and corresponds to $\theta_{cm} \approx 75°$. Simple theoretical arguments involving transformation from the π-N c.m. system, where the differential cross-section is minimum at $\theta_{cm} = 90°$, to the π-nucleus c.m. system, allows an explanation of the angular shift, at least qualitatively.

This conclusion, if confirmed, is of great practical importance. Further study of π-nucleus scattering around the 3/2 3/2 resonance on a series of light nuclei will provide knowledge on the formation and propagation of the Δ_{33} resonance inside a nucleus. The best targets are the lightest ones, since our previous measurements on ^{12}C [1] have shown a completely different behaviour of the differential cross-section with no apparent sign left of a Δ_{33} formation inside this nucleus. This difference can be explained by the strong absorption effect of nuclear "matter" on an object like Δ_{33}. Carbon has already such a great number of absorbing centres that Δ_{33} is readily absorbed before decaying. The smaller number of nucleons in the case of helium leaves it a greater chance to decay.

Of course, it may be wondered why a "classical" phase-shift analysis was not performed instead of going first through a phenomenological fit from which phase shifts are deduced afterwards. There are at least two good reasons for this. First, the parameters entering the phenomenological fit are less numerous than those which are needed in a conventional phase-shift analysis: only four parameters are necessary up to 110 MeV, and six above in the former case, while 3 to 6 partial waves are necessary between 50 and 260 MeV, which means from 6 to 12 parameters, in the latter. Secondly, the parameters involved in the phenomenological fit have a well-defined physical meaning. In particular, the complex parameters t_j are linked to the "visible" zeros of the scattering amplitude. Their real parts show a very regular behaviour as a function of energy (cf. Fig. 9) and their imaginary parts are expected to do the same. This allows one to get some information on their sign, which is not determined in the fit, by using the argument of continuity. The sign ambiguity for Im t_j is not a weakness proper to this type of fit, but is intimately connected with the well-known ambiguities encountered in phase-shift analysis [16]. Both methods should be considered rather complementary as it was shown previously that the reconstructed phase shifts allowed the exclusion of the negative Im t_1 at low energies while, in its turn, a plausible argument about the possible behaviour of Im t_1 allowed the exclusion of some solutions for the phase shifts.

The question now arises as to whether the good description of the data with the phenomenological formula given in Section 5.1 is accidental, and could perhaps fail at higher energies, or for other nuclei. Our belief is that it is not accidental. In this respect, a method, which is known as the amplitude zero analysis, was proposed some years ago by Barrelet [20] as an alternative, but equivalent, method to the more conventional phase-shift analysis. The present phenomenological formula is closely linked, although not α *priori* equivalent, to this formalism. However, a remarkable property of this formula is that in the expansion of the exponential in powers of cos θ, only a few terms are significant at low energy (typically 3 to 4 at 180 MeV) and their number increases with energy in a way similar to the number of partial waves necessary with increasing energy. A careful study of this formula could well be worth the effort.

Acknowledgements

We are greatly indebted to Dr. J.-F. Germond and Dr. C. Wilkin for many fruitful discussions concerning the interpretation of the data. The helium target was built in the Cryogenic Department at the Institut de Physique Nucléaire, Orsay. We are very grateful to its chief, Mr. S. Buhler, and to Mr. J. Mommejat for their devoted assistance. We would like to thank Dr. J.R. Pizzi and his colleagues from the Institut de Physique Nucléaire in Lyon for their help in the calibration of our MWPC at their cyclotron. We thank the CERN Synchro-cyclotron operators. We enjoyed the help of Dr. V. Bobyr during the early part of the experiment and of Dr. E. Labie in the final part.

REFERENCES

[1] F. Binon, P. Duteil, J.P. Garron, J. Gorres, L. Hugon, J.P. Peigneux, C. Schmit, M. Spighel and J.P. Stroot, Nuclear Phys. B17 (1970) 168.

[2] F. Binon, V. Bobyr, P. Duteil, M. Gouanère, L. Hugon, J.P. Peigneux, J. Renuart, C. Schmit, M. Spighel and J.P. Stroot, Nuclear Phys. B33 (1971) 42 and B40 (1972) 608(E).

[3] F. Binon, V. Bobyr, P. Duteil, M. Gouanère, L. Hugon, M. Spighel and J.P. Stroot, Nuclear Instrum. Methods 94 (1971) 27.

[4] M.M. Block, I. Kenyon, J. Keren, D. Koetke, P. Malhotra, R. Walker and H. Winzeler, Phys. Rev. 169 (1968) 1074.

[5] K.M. Crowe, A. Fainberg, J. Miller and A.S.L. Parsons, Phys. Rev. 180 (1969) 1349.

[6] C. Wilkin, C. Cox, J. Domingo, K. Gabathuler, E. Pedroni, J. Rohlin, P. Schwaller and N. Tanner, Nuclear Phys. B62 (1973) 61.

[7] G. Burleson, K. Johnson, J. Calarco, M. Cooper, D. Hagerman, H. Meyer, R. Redwine, I. Halpern, L. Knutson, R. Marss, M. Jakobson and R. Jeppesen, Private communication and 6th Internat. Conf. on High Energy Physics and Nuclear Structure, Santa Fe and Los Alamos, 1975, Abstracts of contributed papers, No. I.D.6;
F. Binon, Meson-nuclear physics - 1976, AIP Conf. Proc. No. 33 (Eds: P.D. Barnes, R.A. Eisenstein and L.S. Kisslinger) (American Institute of Physics, New York, 1976), p. 348.

[8] M. Locher, O. Steinmann and N. Straumann, Nuclear Phys. B27 (1971) 598.

[9] J.F. Germond and C. Wilkin, Private communication and Nuclear Phys. A237 (1975) 477.

[10] R.F. Frosch, J.S. McCarthy, R.E. Rand and M.R. Yearian, Phys. Rev. 160 (1967) 874.

[11] See, for example, M. Locher, Nuclear Phys. B2 (1967) 525.

[12] F. James and M. Roos, Comput. Phys. Commun. 10 (1975) 343.

[13] F. Binon, P. Duteil, M. Gouanère, L. Hugon, J. Jansen, J.P. Lagnaux, H. Palevsky, J.P. Peigneux, M. Spighel and J.P. Stroot, Phys. Rev. Letters 35 (1975) 145.

[14] C.J. Batty, G.T. Squier and G.K. Turner, Nuclear Phys. B67 (1973) 492.

[15] J. Beiner and J.F. Germond, Phys. Letters 46B (1973) 289.

[16] R.R. Silbar and M.M. Sternheim, Phys. Rev. Letters 31 (1973) 941.

[17] A. Gersten, Nuclear Phys. B12 (1969) 537.

[18] M. Abramowitz and I.A. Stegun (eds), Handbook of Mathematical Functions (Dover, New York, 1965), p. 376 and Tables pp. 416-427.

[19] M.E. Nordberg and K.F. Kinsey, Phys. Letters 20 (1966) 692.

[20] E. Barrelet, Nuovo Cimento 8A (1972) 331.

Table 1a

$\pi^- - {}^4He$ differential cross-section at small angles

T = 110 MeV, k = 194.18 MeV/c			
θ_{cm} (deg)	$\|t\|$ $(MeV/c)^2$	$\left(\frac{d\sigma}{d\Omega}\right)_{cm}$ (mb/sr)	$\left(\frac{d\sigma}{d\Omega}\right)^{Coul}_{cm}$ (mb/sr)
4.86	271	382.0 ± 45.0	257.0
5.13	301	348.0 ± 44.0	207.0
5.39	333	282.0 ± 27.0	169.0
5.68	370	231.0 ± 21.0	137.0
5.93	404	247.0 ± 18.0	115.0
6.21	443	200.0 ± 15.0	95.5
6.46	479	168.0 ± 12.0	81.4
6.75	522	168.0 ± 12.0	68.6
7.00	561	159.0 ± 11.0	59.2
7.28	608	132.9 ± 9.2	50.5
7.53	650	114.3 ± 8.0	44.1
7.81	700	121.7 ± 7.9	38.0
8.06	745	112.6 ± 6.4	33.5
8.34	798	107.2 ± 6.1	29.1
8.59	847	104.7 ± 6.5	25.8
8.88	903	95.9 ± 5.6	22.7
9.13	955	98.6 ± 5.6	20.3
9.41	1014	77.6 ± 5.2	17.9
9.68	1073	91.5 ± 10.9	16.0
10.11	1170	84.4 ± 4.7	13.4
10.45	1251	89.5 ± 6.6	11.7
11.20	1436	79.5 ± 4.3	8.83
11.51	1517	65.9 ± 6.3	7.89
12.26	1721	66.7 ± 4.3	6.10
13.28	2016	53.8 ± 5.6	4.40
14.00	2238	48.4 ± 5.0	3.55
14.88	2527	53.1 ± 4.7	2.76
15.59	2774	53.0 ± 2.8	2.27
16.47	3094	49.1 ± 3.3	1.81
18.25	3792	41.3 ± 3.4	1.18
19.13	4163	41.9 ± 4.8	0.970
20.90	4963	41.2 ± 2.1	0.666
21.78	5383	40.4 ± 2.6	0.559
26.20	7750	28.8 ± 2.4	0.252

Table 1a (contd.)

T = 110 MeV, k = 194.18 MeV/c			
θ_{cm} (deg)	$\|t\|$ $(MeV/c)^2$	$\left(\frac{d\sigma}{d\Omega}\right)_{cm}$ (mb/sr)	$\left(\frac{d\sigma}{d\Omega}\right)^{Coul}_{cm}$ (mb/sr)
27.08	8267	30.5 ± 2.6	0.218
28.85	9359	23.8 ± 1.1	0.165
29.73	9923	24.5 ± 2.5	0.144
36.77	15001	19.0 ± 1.2	0.054
37.64	15694	17.9 ± 1.6	0.049

Table 1b

T = 180 MeV, k = 265.45 MeV/c			
θ_{cm} (deg)	$\|t\|$ $(MeV/c)^2$	$\left(\frac{d\sigma}{d\Omega}\right)_{cm}$ (mb/sr)	$\left(\frac{d\sigma}{d\Omega}\right)^{Coul}_{cm}$ (mb/sr)
4.70	473	233.0 ± 30.0	131.0
5.11	560	190.0 ± 25.0	93.7
5.38	620	186.0 ± 14.0	76.2
5.74	705	161.0 ± 17.0	59.8
6.20	824	138.0 ± 10.0	42.9
6.42	882	155.8 ± 9.8	37.4
6.72	968	146.9 ± 9.6	31.0
6.93	1031	122.1 ± 7.9	27.3
7.24	1123	139.4 ± 8.6	22.9
7.45	1190	138.0 ± 8.2	20.4
7.76	1289	129.3 ± 7.8	17.3
7.97	1361	112.0 ± 6.8	15.5
8.27	1467	126.3 ± 7.4	13.3
8.49	1544	126.1 ± 7.0	12.0
8.79	1656	121.3 ± 6.0	10.4
9.01	1738	111.8 ± 6.2	9.40
9.31	1857	106.9 ± 5.5	8.20
9.53	1943	114.3 ± 4.7	7.47
9.83	2069	103.2 ± 6.2	6.57
10.04	2160	108.6 ± 5.7	6.01
10.48	2349	110.2 ± 4.2	5.05
11.00	2587	105.9 ± 4.1	4.13
11.51	2836	111.7 ± 4.2	3.42
11.90	3030	108.9 ± 5.3	2.98
12.18	3173	102.8 ± 4.1	2.70
12.64	3414	114.8 ± 4.5	2.32
12.99	3608	112.7 ± 8.5	2.06
13.61	3955	103.2 ± 4.3	1.70
15.07	4844	93.4 ± 7.4	1.10
15.68	5243	98.3 ± 4.0	0.931
20.25	8705	78.3 ± 6.1	0.305
20.86	9234	77.4 ± 3.2	0.267
25.42	13641	64.2 ± 4.8	0.108
26.03	14294	61.2 ± 2.4	0.096

Table 1c

T = 260 MeV, k = 339.55 MeV/c			
θ_{cm} (deg)	$\|t\|$ $(MeV/c)^2$	$\frac{d\sigma}{d\Omega}_{cm}$ (mb/sr)	$\frac{d\sigma}{d\Omega}^{Coul}_{cm}$ (mb/sr)
3.92	541	203.0 ± 50.0	151.0
4.48	703	132.0 ± 22.0	88.7
4.76	795	141.0 ± 12.0	69.2
5.03	887	95.0 ± 14.0	55.5
5.31	989	100.0 ± 7.9	44.4
5.69	1136	97.9 ± 7.7	33.6
6.25	1372	89.5 ± 3.2	22.8
6.81	1625	91.0 ± 3.2	16.2
7.36	1898	92.4 ± 2.9	11.8
7.91	2193	93.6 ± 2.7	8.73
8.46	2508	96.3 ± 2.7	6.61
9.01	2845	89.0 ± 3.7	5.09
9.56	3202	90.0 ± 2.5	3.97
10.11	3581	91.2 ± 2.5	3.14
10.69	4004	89.6 ± 2.7	2.48
11.17	4370	89.6 ± 3.5	2.06
11.79	4868	92.9 ± 2.6	1.64
12.29	5280	90.0 ± 4.7	1.37
12.90	5822	85.7 ± 3.0	1.11
13.44	6310	83.8 ± 4.4	0.934
13.89	6740	80.2 ± 4.1	0.808
14.54	7380	86.2 ± 4.2	0.662
15.49	8369	86.0 ± 5.8	0.500
16.32	9287	78.5 ± 3.6	0.395
17.19	10295	72.0 ± 3.6	0.312
17.83	11077	74.2 ± 3.6	0.264
20.97	15277	66.9 ± 4.4	0.123
21.80	16495	63.5 ± 2.8	0.101
22.67	17815	61.0 ± 2.8	0.084
23.31	18828	54.7 ± 2.9	0.073
26.45	24128	45.1 ± 3.0	0.038
27.27	25633	45.4 ± 2.0	0.032
28.14	27249	43.9 ± 1.9	0.027
28.78	28483	41.6 ± 3.0	0.024
31.90	34815	32.6 ± 1.6	0.013
32.72	36592	31.9 ± 1.0	0.011
33.58	38487	29.9 ± 0.93	0.010
34.22	39923	26.7 ± 0.90	0.009

Table 2

$\pi^- - {}^4He$ differential cross-sections at large angles

	T = 110 MeV k = 194.18 MeV/c		T = 150 MeV k = 235.90 MeV/c		T = 180 MeV k = 265.45 MeV/c		T = 220 MeV k = 303.23 MeV/c		T = 260 MeV k = 339.55 MeV/c	
θ_{lab} (deg)	θ_{cm} (deg)	$\left(\frac{d\sigma}{d\Omega}\right)_{cm}$ (mb/sr)	θ_{cm} (deg)	$\left(\frac{d\sigma}{d\Omega}\right)_{cm}$ (mb/sr)	θ_{cm} (deg)	$\left(\frac{d\sigma}{d\Omega}\right)_{cm}$ (mb/sr)	θ_{cm} (deg)	$\left(\frac{d\sigma}{d\Omega}\right)_{cm}$ (mb/sr)	θ_{cm} (deg)	$\left(\frac{d\sigma}{d\Omega}\right)_{cm}$ (mb/sr)
10.0			10.75	97.7 ± 4.0			10.92	108.7 ± 3.6		
12.0					12.99	91.7 ± 5.4			13.22	87.4 ± 2.2
12.5			13.44	87.4 ± 1.9						
15.0			16.12	83.2 ± 2.6			16.38	94.5 ± 2.2		
17.5	18.63	43.4 ± 1.0	18.80	76.8 ± 2.3						
20.0			21.48	68.5 ± 2.2			21.82	77.8 ± 2.2		
25.0			26.82	52.1 ± 1.7			27.24	57.0 ± 1.5		
27.5	29.23	28.1 ± 0.7								
30.0			32.16	42.8 ± 1.3	32.37	43.1 ± 0.7	32.65	37.7 ± 1.4	32.92	29.2 ± 0.5
35.0	37.14	18.4 ± 0.5	37.47	30.1 ± 0.8	37.71	29.7 ± 0.4	38.03	26.2 ± 0.4	38.35	17.9 ± 0.3
40.0	42.40	12.2 ± 0.7	42.76	21.3 ± 0.8	43.03	18.8 ± 0.5	43.39	15.6 ± 0.6	43.74	10.5 ± 0.4
45.0	47.64	9.81 ± 0.71	48.03	14.3 ± 0.7	48.33	11.4 ± 0.4	48.72	8.53 ± 0.49	49.10	5.30 ± 0.22
50.0	52.85	6.17 ± 0.48	53.28	7.49 ± 0.37	53.60	6.15 ± 0.30	54.02	4.86 ± 0.36	54.43	2.23 ± 0.15
55.0	58.04	3.25 ± 0.33	58.50	5.07 ± 0.30	58.84	3.05 ± 0.15	59.29	1.85 ± 0.19	59.72	0.792 ± 0.090
60.0	63.21	1.90 ± 0.28	63.69	2.21 ± 0.15	64.05	0.99 ± 0.13	64.52	0.591 ± 0.080	64.98	0.269 ± 0.046
65.0	68.36	1.48 ± 0.21	68.86	0.83 ± 0.12	69.23	0.151 ± 0.042	69.71	0.064 ± 0.016	70.19	0.045 ± 0.011
70.0	73.47	0.77 ± 0.15	73.99	0.56 ± 0.11	74.37	0.130 ± 0.036	74.87	0.000 ± 0.007	75.36	0.041 ± 0.025
75.0	78.56	0.71 ± 0.16	79.09	0.52 ± 0.07	79.48	0.207 ± 0.048	79.99	0.089 ± 0.041	80.49	0.013 ± 0.008
80.0	83.63	1.23 ± 0.21	84.16	0.82 ± 0.12	84.55	0.397 ± 0.057	85.07	0.098 ± 0.028	85.58	0.051 ± 0.016

Table 2 (contd.)

	T = 110 MeV k = 194.18 MeV/c		T = 150 MeV k = 235.90 MeV/c		T = 180 MeV k = 265.45 MeV/c		T = 220 MeV k = 303.23 MeV/c		T = 260 MeV k = 339.55 MeV/c	
θ_{lab} (deg)	θ_{cm} (deg)	$\left(\frac{d\sigma}{d\Omega}\right)_{cm}$ (mb/sr)	θ_{cm} (deg)	$\left(\frac{d\sigma}{d\Omega}\right)_{cm}$ (mb/sr)	θ_{cm} (deg)	$\left(\frac{d\sigma}{d\Omega}\right)_{cm}$ (mb/sr)	θ_{cm} (deg)	$\left(\frac{d\sigma}{d\Omega}\right)_{cm}$ (mb/sr)	θ_{cm} (deg)	$\left(\frac{d\sigma}{d\Omega}\right)_{cm}$ (mb/sr)
85.0	88.66	1.38 ± 0.21	89.20	1.08 ± 0.13	89.59	0.407 ± 0.056	90.11	0.193 ± 0.025	90.62	0.060 ± 0.013
90.0	93.67	2.13 ± 0.26	94.20	1.41 ± 0.15	94.60	0.613 ± 0.070	95.12	0.150 ± 0.049	95.62	0.048 ± 0.018
95.0	98.65	2.64 ± 0.42	99.18	1.74 ± 0.16	99.57	0.660 ± 0.073	100.08	0.231 ± 0.059	100.58	0.011 ± 0.005
100.0	103.60	2.45 ± 0.26	104.11	1.74 ± 0.17	104.50	0.687 ± 0.098	105.00	0.068 ± 0.041	105.50	0.017 ± 0.010
105.0	108.52	3.06 ± 0.28	109.03	1.85 ± 0.16	109.40	0.477 ± 0.040	109.89	0.112 ± 0.030	110.37	0.005 ± 0.006
110.0	113.42	3.81 ± 0.33	113.91	1.91 ± 0.16	114.27	0.490 ± 0.066	114.74	0.068 ± 0.024	115.21	0.016 ± 0.015
115.0	118.29	3.98 ± 0.39	118.76	1.73 ± 0.19	119.11	0.293 ± 0.046	119.56	0.057 ± 0.019	120.00	0.000 ± 0.011
120.0	123.14	4.06 ± 0.17	123.59	1.70 ± 0.19	123.91	0.348 ± 0.023	124.35	0.072 ± 0.021	124.77	0.015 ± 0.010
125.0	127.96	4.22 ± 0.44	128.38	1.62 ± 0.18	128.69	0.370 ± 0.068	129.10	0.045 ± 0.033	129.49	0.030 ± 0.012
130.0	132.76	3.71 ± 0.43	133.16	1.41 ± 0.17	133.44	0.372 ± 0.062	133.82	0.248 ± 0.035	134.19	0.036 ± 0.012
135.0	137.54	4.44 ± 0.42	137.91	0.90 ± 0.15	138.17	0.341 ± 0.056	138.52	0.209 ± 0.060		
140.0	142.31	4.72 ± 0.50	142.64	1.11 ± 0.16	142.88	0.421 ± 0.072	143.19	0.230 ± 0.058		
144.0	146.10	3.59 ± 0.28	146.40	1.26 ± 0.11	146.62	0.479 ± 0.036	146.91	0.215 ± 0.044	147.19	0.070 ± 0.025
180.0	180.00	5.09 ± 1.67	180.00	1.91 ± 0.64	180.00	1.90 ± 0.45	180.00	0.58 ± 0.18	180.00	0.251 ± 0.089

Table 3

π^--^{4}He total elastic, total inelastic, and total cross-sections. π^--^{4}He elastic differential cross-section and total inelastic differential cross-section at 0°.
[Values in parenthesis are obtained by interpolation (see Section 5)]

T (MeV)	σ_{tot} (mb)	σ_{tot}^{el} (mb)	σ_{tot}^{inel} (mb)	$\sigma_{tot}^{el}/\sigma_{tot}^{inel}$	$\left[\frac{d\sigma}{d\Omega}(0°)\right]_{el}$ (mb/sr)	$\left[\frac{d\sigma}{d\Omega}(0°)\right]_{inel}$ (mb/sr)
67.0	107.5 ± 0.9	38.2 ± 1.8	69.3 ± 2.0	0.551 ± 0.030	9.2 ± 1.1	12.1 ± 0.9
85.5	172.1 ± 1.8				(21.5 ± 1.7)	34.4 ± 3.0
110.0	242.6 ± 2.6	80.1 ± 2.8	162.5 ± 3.8	0.493 ± 0.021	48.6 ± 2.1	25.5 ± 4.7
130.0	292.1 ± 3.2				(70.6 ± 1.9)	26.6 ± 5.9
150.0	319.8 ± 3.1	112.7 ± 1.7	207.1 ± 3.5	0.544 ± 0.012	94.9 ± 2.8	24.5 ± 4.5
165.0	332.2 ± 3.2				(113.6 ± 2.2)	21.7 ± 4.4
180.0	323.7 ± 3.9	111.8 ± 3.1	211.9 ± 5.0	0.528 ± 0.019	120.2 ± 2.9	23.6 ± 7.6
200.0	308.9 ± 2.7				(126.5 ± 2.2)	25.4 ± 2.6
220.0	286.5 ± 3.3	104.9 ± 3.1	181.6 ± 4.5	0.578 ± 0.022	122.9 ± 2.9	25.4 ± 6.1
260.0	233.6 ± 3.7	82.9 ± 3.2	150.7 ± 4.9	0.550 ± 0.028	113.3 ± 4.0	24.2 ± 7.9
285.0	213.1 ± 2.5				(112.1 ± 4.1)	18.6 ± 4.5
110.0 [a]	211.7 ± 1.0					

a) π^+-^{4}He total cross-section.

Table 4

Fitted values for the parameters of f_N (see text)

T (MeV)	k (fm^{-1})	σ_{tot} (fm^2)	ρ	R'_S (fm)	Re $(1 - z_1)$	Im $(1 - z_1)$	Re $(1 - z_2)$	Im $(1 - z_2)$	n	χ^2
51	0.6259	(6.0 ± 0.5) a)	2.14 ± 0.21	1.439 ± 0.038	0.670 ± 0.005	0.204 ± 0.005			11	20
60	0.6866	(8.65 ± 3.1) a)	1.558 ± 0.076	1.425 ± 0.017	0.698 ± 0.002	0.191 ± 0.002			11	33
68	0.7381	11.10 ± 0.22	1.106 ± 0.046	1.393 ± 0.029	0.714 ± 0.005	0.198 ± 0.004			11	17
75	0.7816	(13.50 ± 0.23) a)	0.951 ± 0.035	1.475 ± 0.014	0.716 ± 0.003	0.202 ± 0.002			11	26
110	0.9840	24.26 ± 0.26	0.558 ± 0.047	1.684 ± 0.018	0.704 ± 0.009	0.185 ± 0.010			114	125
150	1.1954	31.98 ± 0.31	0.148 ± 0.078	1.233 ± 0.104	0.729 ± 0.007	0.137 ± 0.010	$2.14^{+0.88}_{-0.22}$	-0.529 ± 0.092	25	29
180	1.3452	32.37 ± 0.39	-0.028 ± 0.031	1.309 ± 0.061	0.708 ± 0.008	0.077 ± 0.012	1.614 ± 0.024	-0.370 ± 0.055	109	128
220	1.5366	28.65 ± 0.33	-0.019 ± 0.147	1.262 ± 0.035	0.721 ± 0.005	0.020 ± 0.011	1.452 ± 0.023	-0.202 ± 0.031	23	40
260	1.7207	23.36 ± 0.37	-0.321 ± 0.028	1.342 ± 0.032	0.726 ± 0.011	0.064 ± 0.023	1.350 ± 0.026	-0.120 ± 0.051	107	92

a) Values obtained by extrapolation or interpolation -- see text. n is the number of degrees of freedom in the fits.

Table 5

Results of the "reconstructed" phase-shift analysis

T (MeV)		$\ell = 0$ (S)	$\ell = 1$ (P)	$\ell = 2$ (D)	$\ell = 3$ (F)	$\ell = 4$ (G)
51	2δ (deg)	-17.2 ± 1.7	17.3 ± 1.6	1.90 ± 0.19	0.110 ± 0.014	0.004 ± 0.001
	η	0.873 ± 0.026	0.985 ± 0.012	0.994 ± 0.001	0.999 ± 0.001	0.999 ± 0.001
60	2δ (deg)	-19.5 ± 0.9	22.1 ± 0.9	2.74 ± 0.13	0.186 ± 0.010	0.008 ± 0.001
	η	0.899 ± 0.013	0.933 ± 0.007	0.984 ± 0.001	0.998 ± 0.001	0.999 ± 0.001
68	2δ (deg)	-21.2 ± 1.0	25.1 ± 0.9	3.21 ± 0.15	0.240 ± 0.020	0.012 ± 0.002
	η	0.921 ± 0.014	0.863 ± 0.008	0.972 ± 0.001	0.998 ± 0.001	0.999 ± 0.001
75	2δ (deg)	-23.3 ± 0.8	28.9 ± 0.9	4.49 ± 0.15	0.416 ± 0.018	0.026 ± 0.001
	η	0.906 ± 0.012	0.813 ± 0.007	0.953 ± 0.001	0.995 ± 0.001	0.999 ± 0.001
110	2δ (deg)	-29.1 ± 3.7	50.4 ± 3.0	12.8 ± 0.9	2.17 ± 0.15	0.288 ± 0.022
	η	0.762 ± 0.044	0.551 ± 0.031	0.798 ± 0.005	0.958 ± 0.001	0.994 ± 0.001
150	2δ (deg)	-65.0 ± 37.0	72.0 ± 29.0	13.8 ± 7.9	1.5 ± 1.1	0.17 ± 0.16
	η	0.46 ± 0.25	0.27 ± 0.16	0.49 ± 0.10	0.874 ± 0.026	0.981 ± 0.005
180	2δ (deg)	81.0 ± 18.0	41.0 ± 28.0	0 ± 4.6	-0.75 ± 0.66	-0.19 ± 0.12
	η	0.365 ± 0.085	0.105 ± 0.051	0.321 ± 0.042	0.773 ± 0.008	0.953 ± 0.004
220	2δ (deg)	31.0 ± 32.0	59.0 ± 72.0	-2.0 ± 16.0	-1.2 ± 2.6	-0.31 ± 0.54
	η	0.291 ± 0.121	0.059 ± 0.106	0.255 ± 0.035	0.707 ± 0.009	0.928 ± 0.003
260	2δ (deg)	71.3 ± 9.2	-74.9 ± 9.0	-32.2 ± 5.2	-8.30 ± 1.34	-2.02 ± 0.32
	η	0.483 ± 0.085	0.311 ± 0.063	0.381 ± 0.032	0.678 ± 0.013	0.895 ± 0.004

Table 6

Dependence of the "reconstructed" phase-shift parameter on the sign of Im $(1 - z_i)$

	Im $(1 - z_1)$	+				−			
	Im $(1 - z_2)$	−		+		+		−	
T (MeV)	ℓ	δ (deg)	η	δ (deg)	η	δ (deg)	η	δ (deg)	η
150	0	-32	0.46	-6	0.44	30	0.73	14	0.55
	1	36	0.27	-2	0.03	19	0.06	43	0.31
	2	7	0.49	10	0.51	3	0.47	0	0.45
180	0	40	0.36	11	0.05	-39	0.30	-30	0.10
	1	21	0.11	-38	0.22	-27	0.15	37	0.17
	2	0	0.32	2	0.32	-3	0.32	-4	0.32
220	0	16	0.29	-3	0.24	-9	0.27	13	0.26
	1	28	0.06	-39	0.13	-37	0.11	35	0.07
	2	-1	0.26	-2	0.25	-3	0.26	-3	0.26
260	0	36	0.48	36	0.44	29	0.37	32	0.38
	1	-37	0.31	-37	0.38	-37	0.31	-37	0.24
	2	-16	0.38	-17	0.39	-17	0.40	-17	0.39

Figure captions

Fig. 1 : Sketch of the double achromatic spectrometer with the position of counters. A_1, A_2, B: beam defining counters; A_1' and A_2': "anticounters"; H_1 and H_2: 7-channel wall hodoscope and 63-channel final hodoscope, respectively; D: differential Čerenkov counter (DISC); T: target position; S: lead shielding.

Fig. 2 : π^--^{4}He elastic scattering differential cross-sections versus θ_{cm}, the pion scattering angle in the c.m. system. Optical points (*) on the vertical axis show the value of $(k/4\pi)\ |\mathrm{Im}\ f|^2$ as deduced from the measured total cross-sections. Only part of the forward data are shown for the sake of clarity. The curves result from fits by a formula given in the text.

Fig. 3 : π^--^{4}He elastic differential cross-sections versus $t/t_{max} = (1 - \cos\theta_{cm})/2$. The points (*) on the vertical axis are the optical points. Only the "large" angle data are shown for the sake of clarity. The curves result from fits by a formula given in the text.

Fig. 4 : $(d\sigma/d\Omega)_{cm} - (d\sigma/d\Omega)_{cm}^{Coul}$ versus -t, the squared four-momentum transfer. The straight lines (dashed curves) are the "pure" nuclear differential cross-sections. The continuous curves result from fits by a formula given in the text.

Fig. 5 : π^--^{4}He total cross-section, total elastic cross-section and total inelastic cross-section versus the π^- energy in the laboratory. Squares, deduced from data of Crowe et al. [5]; crosses, Wilkin et al. [6]. The solid lines are a guide for the eye only. The dashed curve is a theoretical prediction by Locher et al. [8]. The only point measured with π^+ at 110 MeV is also displayed.

Fig. 6 : Elastic differential cross-section at 0° and inelastic differential cross-section at 0° integrated over all inelastic channels, as a function of the pion energy in the laboratory. The curves are a guide for the eye only.

Fig. 7 : Real part of the forward-scattering amplitude versus T, the pion kinetic energy in the laboratory. The curves were calculated from the forward dispersion relation by Wilkin et al. [6] (dashed curve) and by Batty et al. [14] (full curve).

Fig. 8 : Square of the effective r.m.s. strong interaction radius versus $1/k^2$, where k is the centre-of-mass momentum. The two straight lines are the results of a linear least squares fit to all the data (full line) and to the five lower points only (dashed curve). The encircled point on the vertical axis is the value of the r.m.s. matter-radius of ^{4}He, squared.

Fig. 9 : Fitted values for the real part of the parameters t_1 and t_2 (see text) and their physical limit as a function of the pion kinetic energy in the laboratory.

Fig. 10 : Fitted values for the imaginary part of the parameter t_1 (see text), as a function of the pion kinetic energy in the laboratory. Opposite sign values are represented above 110 MeV, resulting from a sign ambiguity in that region. Both curves represent a "plausible" behaviour of the imaginary part versus the energy (see text).

Fig. 11 : Results of the "reconstructed" phase-shift analysis (see text) for the first four partial waves only. (1: 24 MeV; 2: 51 MeV; 3: 60 MeV; 4: 68 MeV; 5: 75 MeV; 6: 110 MeV; 7: 150 MeV; 8: 180 MeV; 9: 220 MeV; 10: 260 MeV.)

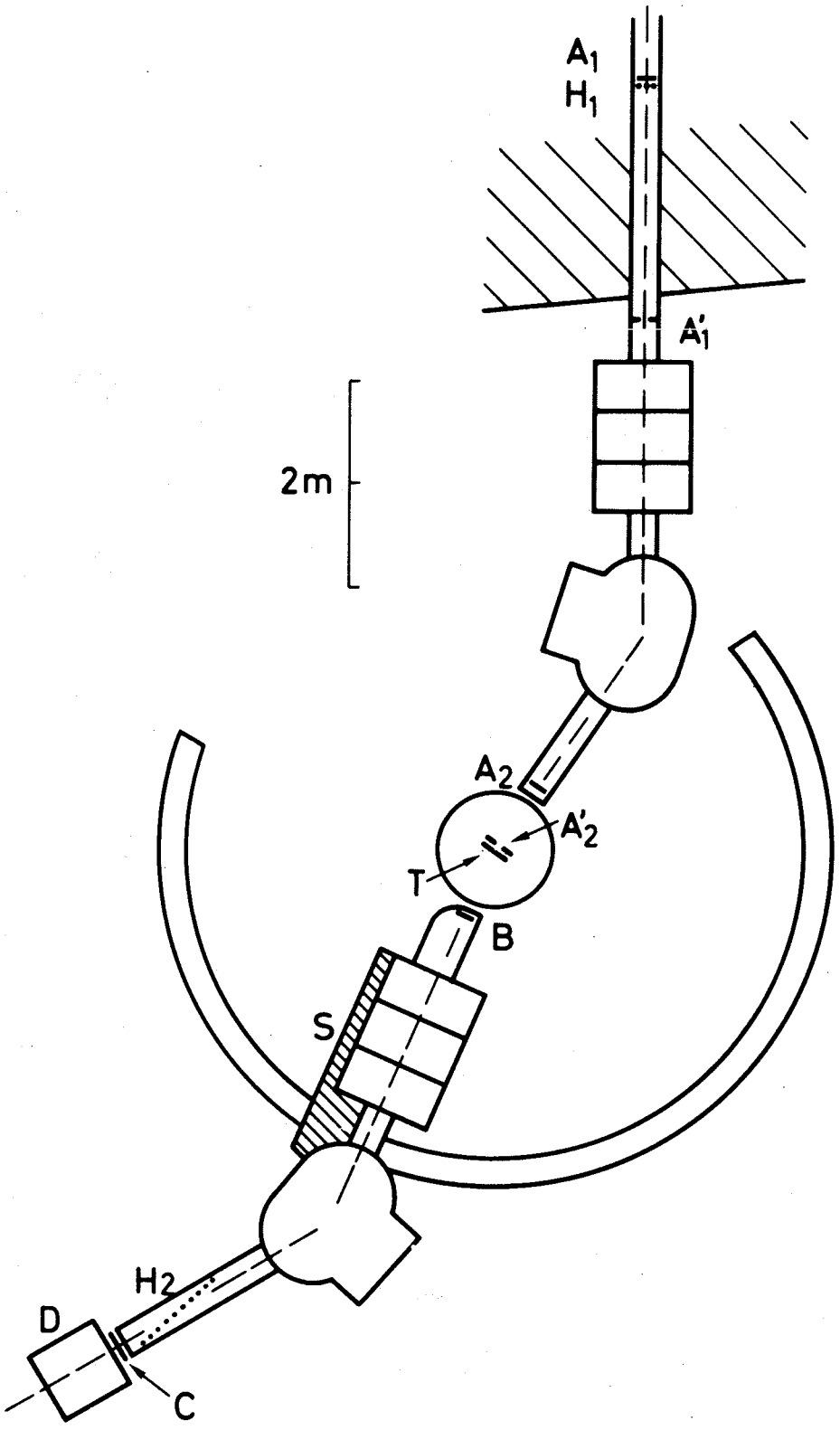

Fig. 1

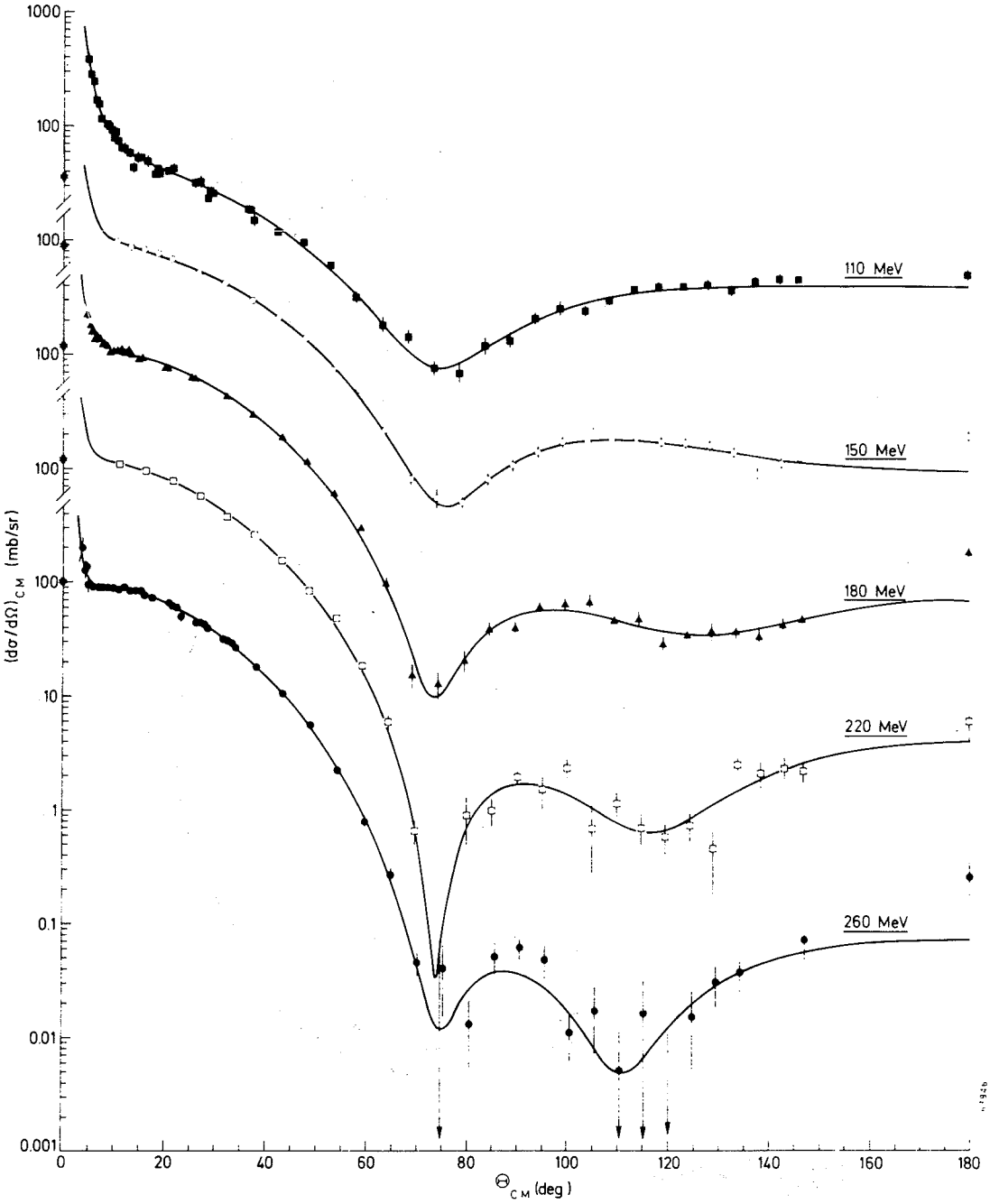
1000
100
100
100
100
100
10
1
0.1
0.01
0.001
(dσ/dΩ)C M (mb/sr)
110 MeV
150 MeV
180 MeV
220 MeV
260 MeV
0
20
40
60
80
100
120
140
160
180
ΘC M (deg)

Fig. 2

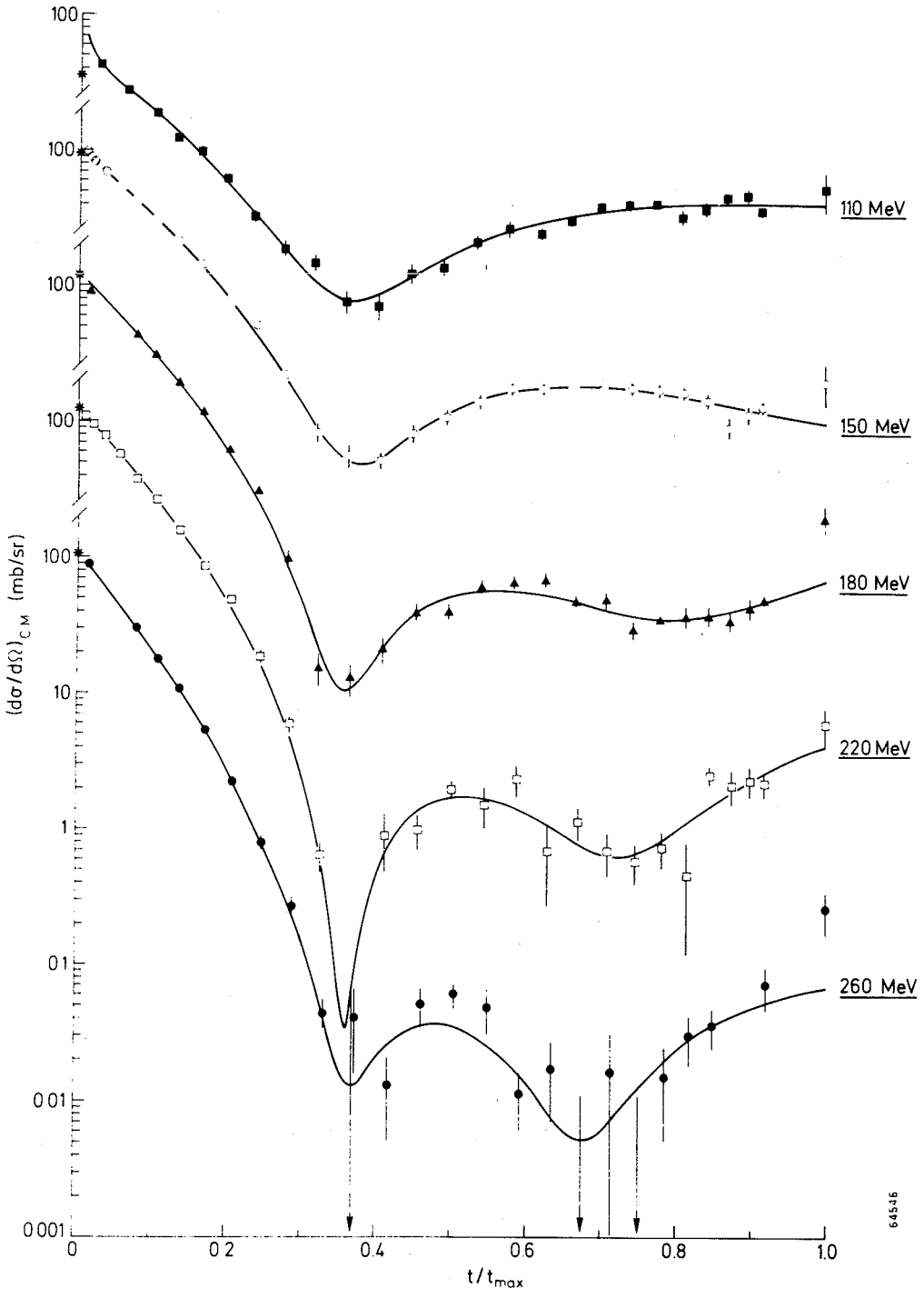
100
100
100
100
100
10
1
01
0 01
0 001
110 MeV
150 MeV
180 MeV
220 MeV
260 MeV
$(d\sigma/d\Omega)_{CM}$ (mb/sr)
0
0 2
0.4
0.6
0.8
1.0
t/t_{max}
64546

Fig. 3

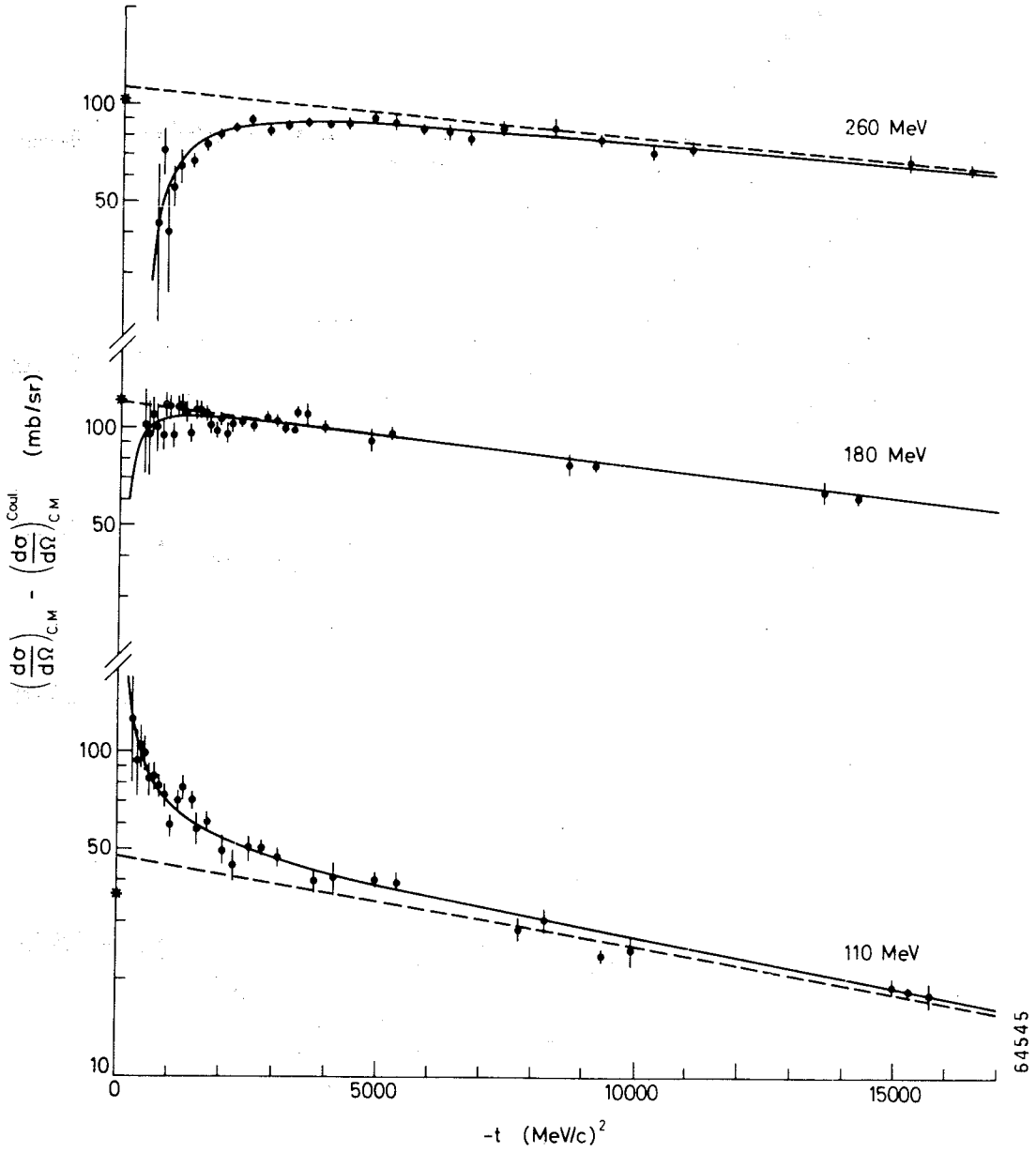
260 MeV
180 MeV
110 MeV
100
50
100
50
100
50
10
0
5000
10000
15000
-t (MeV/c)²
(dσ/dΩ)c.m - (dσ/dΩ)c.m Coul (mb/sr)
64545

Fig. 4

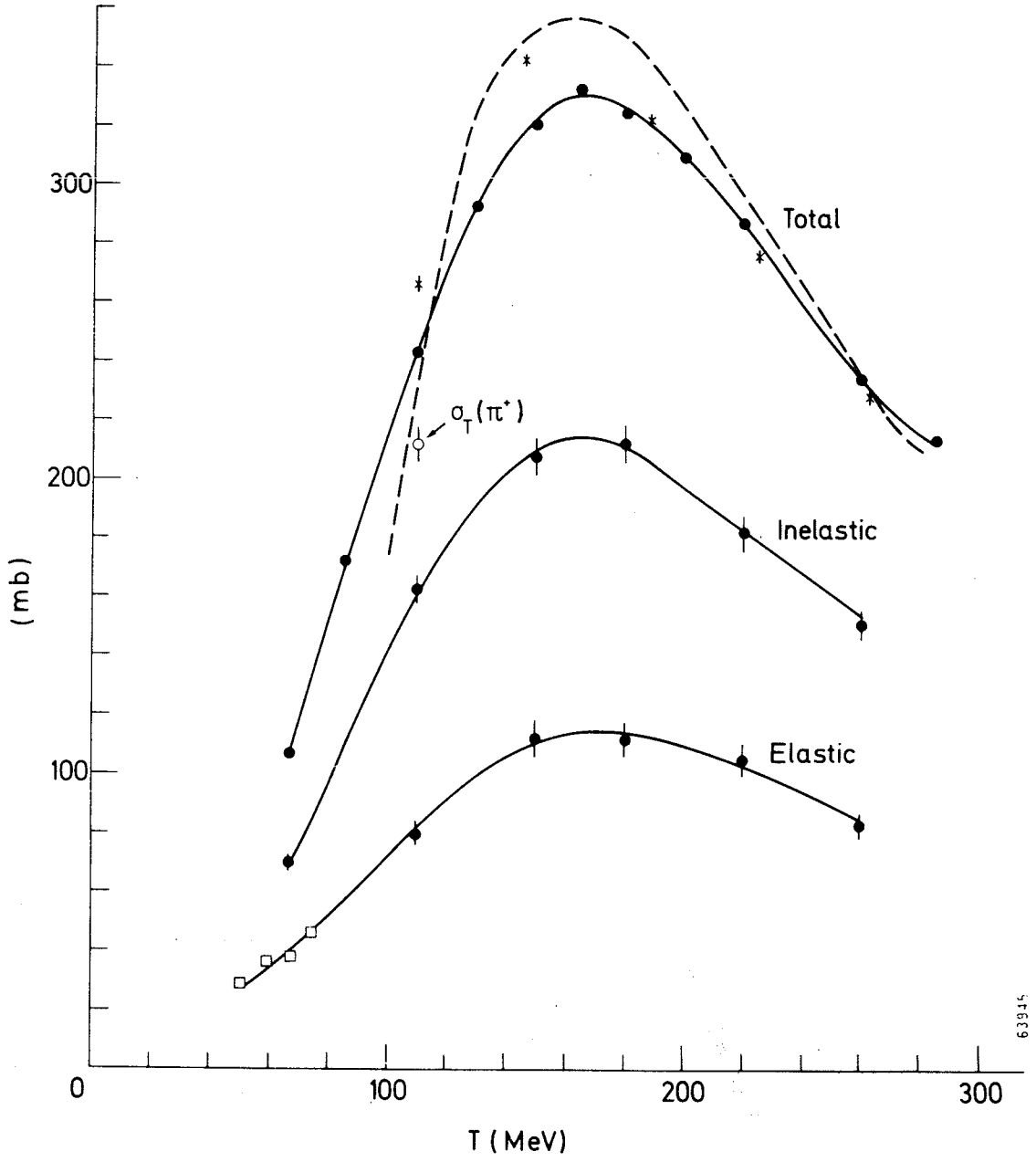
300
200
100
0
(mb)
Total
$\sigma_T(\pi^+)$
Inelastic
Elastic
100
200
300
T (MeV)

Fig. 5

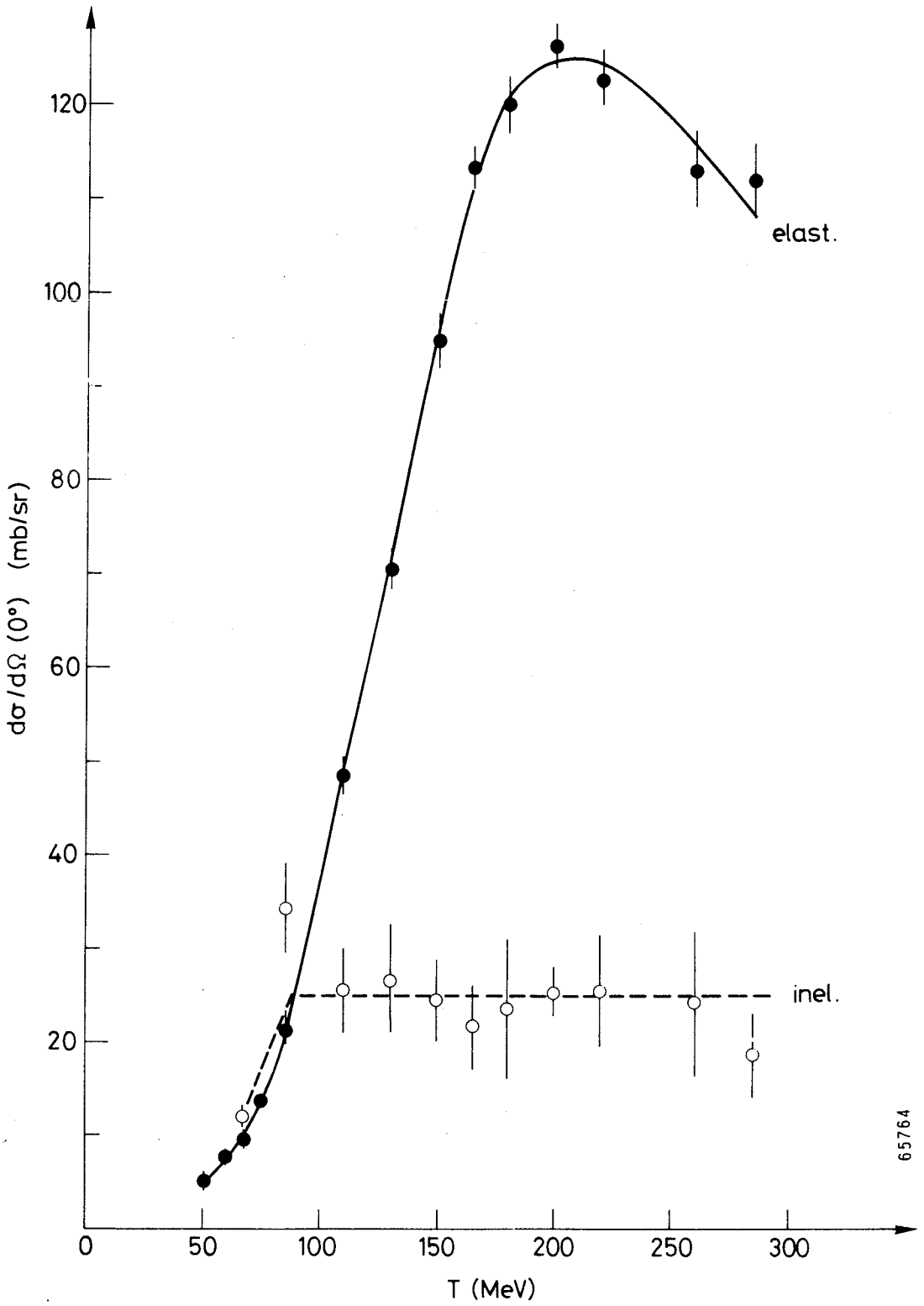
120
100
80
60
40
20
dσ/dΩ (0°) (mb/sr)
elast.
inel.
0
50
100
150
200
250
300
T (MeV)
65764

Fig. 6

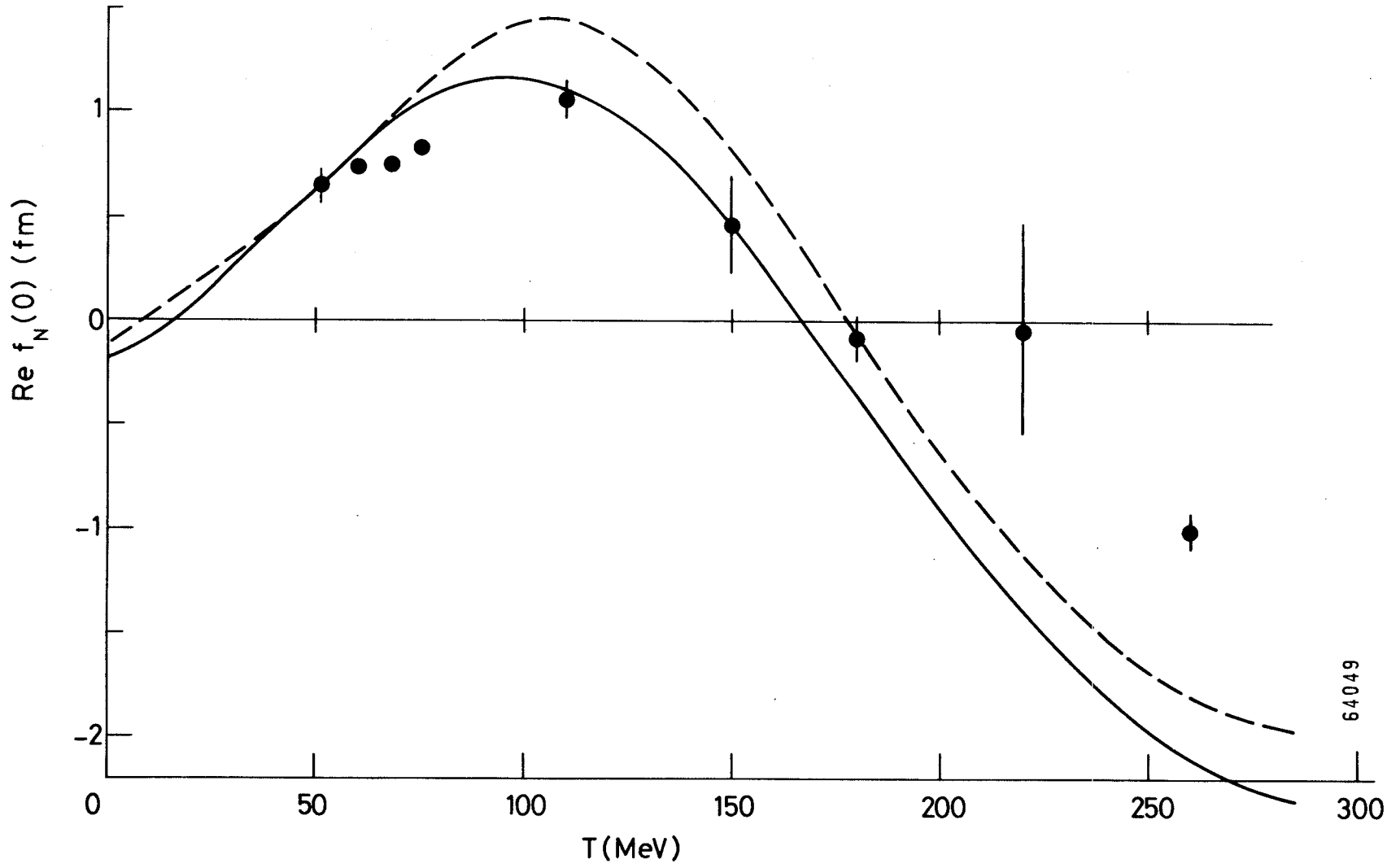

Fig. 7

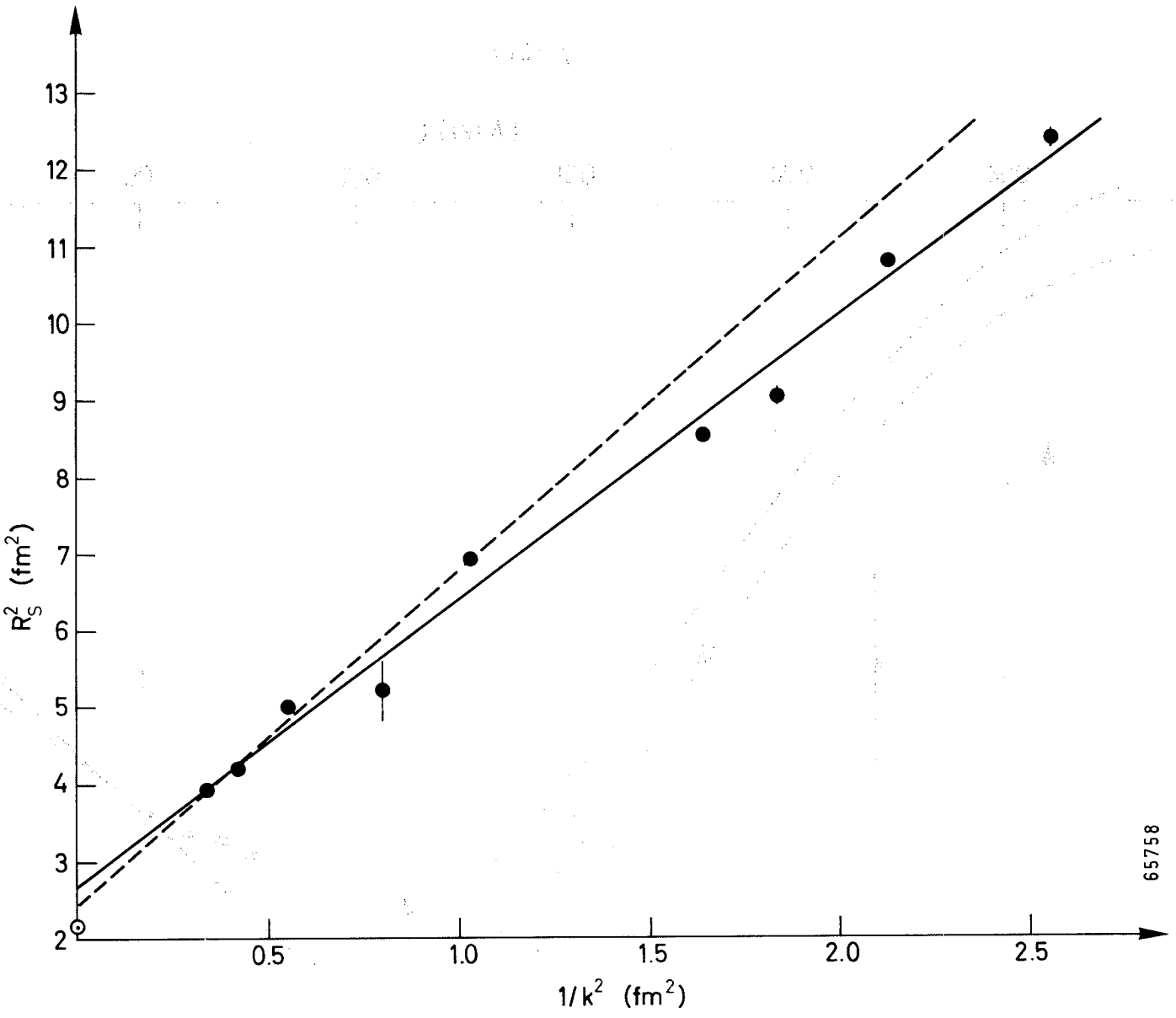

Fig. 8

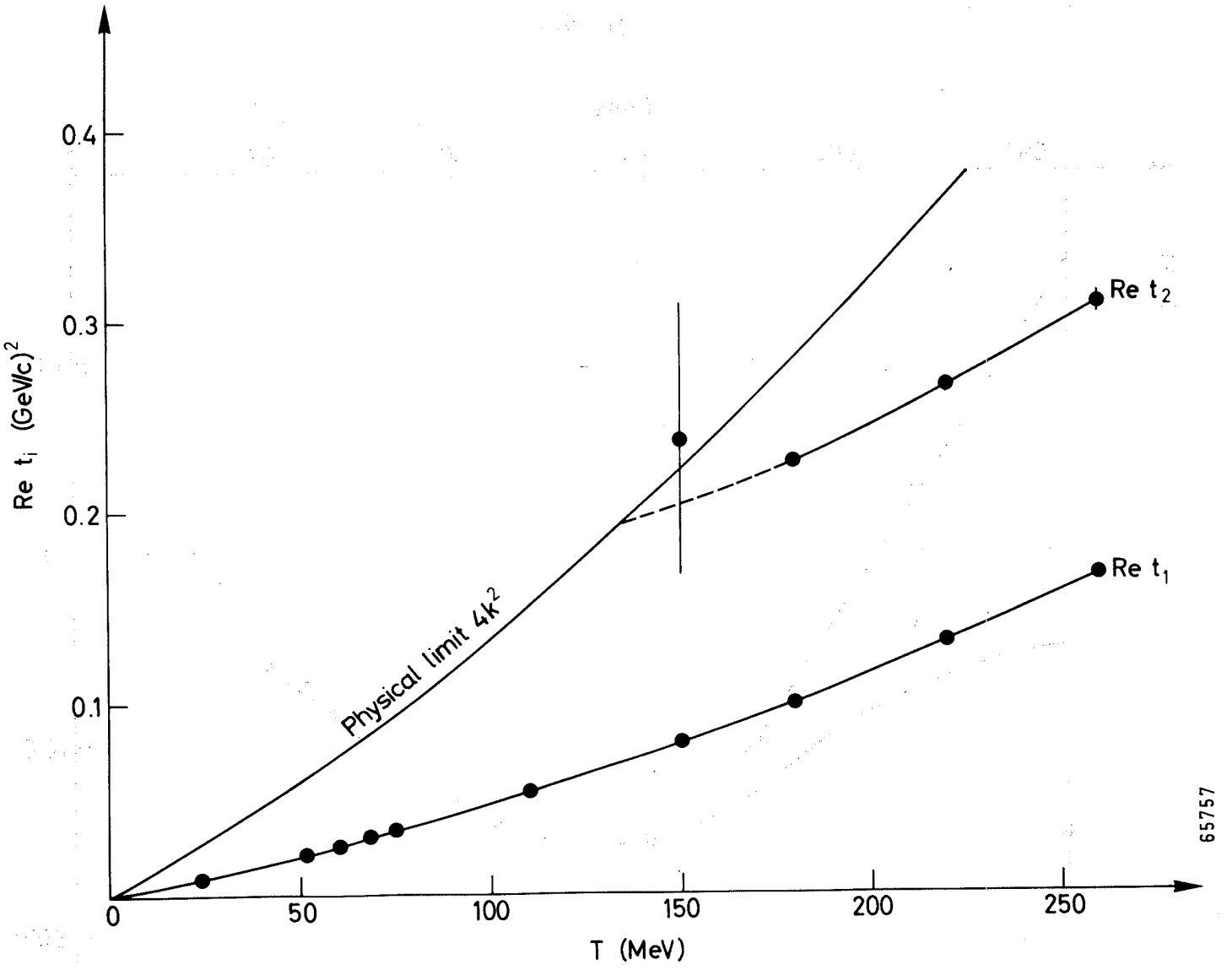
0.4
0.3
0.2
0.1
Re t_l (GeV/c)^2
Physical limit $4k^2$
Re t_2
Re t_1
0
50
100
150
200
250
T (MeV)
65757

Fig. 9

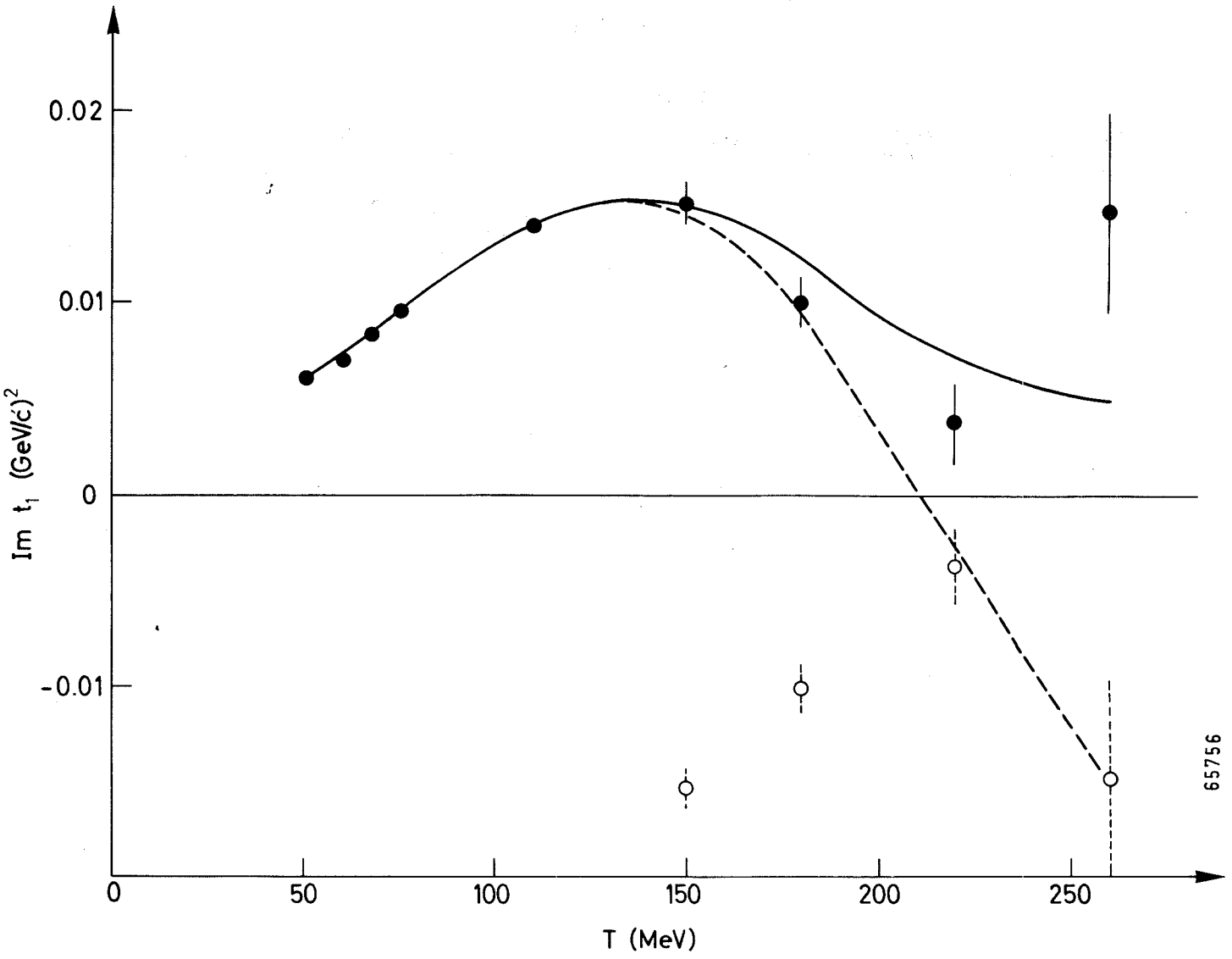

Fig. 10

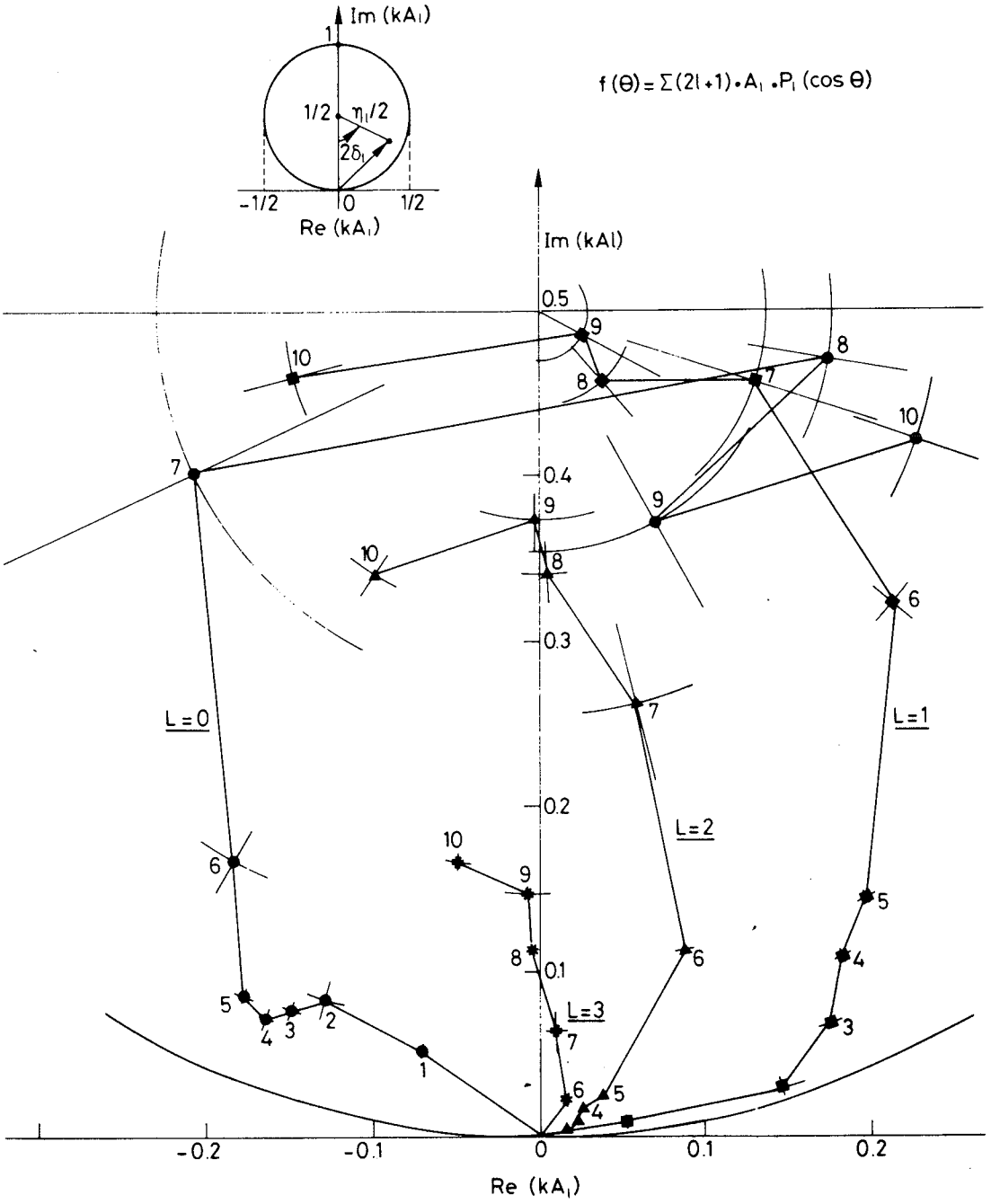
Im (kA$_l$)
1
1/2
η_l/2
$2\delta_l$
-1/2
0
1/2
Re (kA$_l$)
$f(\theta) = \Sigma(2l+1) \cdot A_l \cdot P_l(\cos\theta)$
Im (kAl)
0.5
0.4
0.3
0.2
0.1
L=0
L=1
L=2
L=3
-0.2
-0.1
0
0.1
0.2
Re (kA$_l$)
65759

Fig. 11